# Stromal Reprogramming by FAK Inhibition Overcomes Radiation Resistance to Allow for Immune Priming and Response to Checkpoint Blockade

Varintra E. Lander[1,2], Jad I. Belle[1], Natalie L. Kingston[1,2], John M. Herndon[3], Graham D. Hogg[1,2], Xiuting Liu[1], Liang-I Kang[2], Brett L. Knolhoff[1], Savannah J. Bogner[1], John M. Baer[1], Chong Zuo[1], Nicholas C. Borcherding[2], Daniel P. Lander[4], Cedric Mpoy[5], Jalen Scott[5], Michael Zahner[5], Buck E. Rogers[5], Julie K. Schwarz[5,6,7], Hyun Kim[5,7], and David G. DeNardo[1,2,7]

**ABSTRACT**

The effects of radiotherapy (RT) on tumor immunity in pancreatic ductal adenocarcinoma (PDAC) are not well understood. To better understand if RT can prime antigen-specific T-cell responses, we analyzed human PDAC tissues and mouse models. In both settings, there was little evidence of RT-induced T-cell priming. Using *in vitro* systems, we found that tumor–stromal components, including fibroblasts and collagen, cooperate to blunt RT efficacy and impair RT-induced interferon signaling. Focal adhesion kinase (FAK) inhibition rescued RT efficacy *in vitro* and *in vivo*, leading to tumor regression, T-cell priming, and enhanced long-term survival in PDAC mouse models. Based on these data, we initiated a clinical trial of defactinib in combination with stereotactic body RT in patients with PDAC (NCT04331041). Analysis of PDAC tissues from these patients showed stromal reprogramming mirroring our findings in genetically engineered mouse models. Finally, the addition of checkpoint immunotherapy to RT and FAK inhibition in animal models led to complete tumor regression and long-term survival.

**SIGNIFICANCE:** Checkpoint immunotherapeutics have not been effective in PDAC, even when combined with RT. One possible explanation is that RT fails to prime T-cell responses in PDAC. Here, we show that FAK inhibition allows RT to prime tumor immunity and unlock responsiveness to checkpoint immunotherapy.

## INTRODUCTION

Pancreatic ductal adenocarcinoma (PDAC) is a highly lethal malignancy with a poor 5-year survival rate (1). Currently, complete surgical resection is the only potentially curative treatment, but 85% to 90% of patients are diagnosed at unresectable stages (2). Although recent advances in diagnosis, chemotherapy, and radiotherapies (RT) have improved patient survival, these treatments have not been proven to be curative (3, 4). For many patients with locally advanced PDAC, RT does not achieve resectability, and metastatic PDAC is incurable (2, 5–9). Additionally, to date there are no proven effective immunotherapies for the treatment of PDAC.

Oncogenic mutations in *KRAS*, as well as frequent loss in tumor suppressors such as *TP53* (p53) or *CDKN2A* (*INK4a*), drive PDAC initiation, progression, treatment resistance, and metastatic spread (10). *KRAS* accomplishes this through tumor-intrinsic changes in cellular signaling and metabolism, while promoting tumor-permissive interactions with surrounding stroma (10). This fibrotic desmoplastic stroma, composed of dense collagen-rich extracellular matrix (ECM)

and cancer-associated fibroblasts (CAF), likely contributes to PDAC's resistance to therapy (2, 11–18). Although checkpoint immunotherapies have been groundbreaking in many solid malignancies (19–21), they have not been effective in PDAC (2, 22, 23). Similarly, combination treatments of immunotherapies with the standard-of-care chemotherapy or RT, which are aimed at priming antitumor immunity and unlock immunotherapies, have not been tremendously efficacious in gastrointestinal tumors (24–26). Thus, understanding why RT fails to prime antitumor immunity in PDAC is important.

The recalcitrant nature of PDAC has been linked in part to its unique tumor microenvironment (TME). In this TME, complex communication between the malignant tumor cells and the nonmalignant tumor stroma plays a significant role in dictating PDAC's resistance to therapy (2, 11–13). Further complicating things, PDAC has a very heterogeneous CAF population, which plays diverse roles and contributes to divergent treatment outcomes (14, 27–29). Additionally, PDAC's fibrotic stroma contributes to poor drug delivery and deprived infiltration of antitumor immune cells. These two aspects of the PDAC TME have been confirmed as drivers of PDAC resistance to both chemotherapies and immunotherapies (30–33). However, it is unclear how PDAC-associated fibrosis and CAFs might affect the efficacy of RT and if this affects RT-induced immune priming.

Historically, studies have focused on RT as a direct tool to damage proliferating tumor cells, which leads to the accumulation of double-strand DNA breaks and cellular death (34). However, recent studies have shown that numerous extrinsic factors, including matrix stiffness, can dampen sensitivity to DNA-damaging agents and their subsequent DNA-repair mechanisms (35, 36). In addition to its direct effect on tumor cells, RT can also prime antitumor immunity by releasing tumor-derived antigens and danger signals. This likely plays a critical role in long-term RT efficacy in multiple cancer types (37). Nevertheless, it remains unclear if these immune priming effects of RT are intact in highly fibrotic cancers such as PDAC.

[1]Department of Medicine, Washington University School of Medicine, St. Louis, Missouri. [2]Department of Pathology and Immunology, Washington University School of Medicine, St. Louis, Missouri. [3]Department of Surgery, Washington University School of Medicine, St. Louis, Missouri. [4]Department of Otolaryngology, Washington University School of Medicine, St. Louis, Missouri. [5]Department of Radiation Oncology, Washington University School of Medicine, St. Louis, Missouri. [6]Department of Cell Biology and Physiology, Washington University School of Medicine, St. Louis, Missouri. [7]Siteman Cancer Center, Washington University School of Medicine, St. Louis, Missouri.

**Note:** H. Kim and D.G. DeNardo are co-senior authors.

**Corresponding Authors:** David G. DeNardo, Department of Medicine, 425 South Euclid Avenue, St. Louis, MO 63110. Phone: 314-362-9524; E-mail: ddenardo@wustl.edu; and Hyun Kim, Washington University in St. Louis School of Medicine, Radiation Oncology, St. Louis, MO 63110. E-mail: kim.hyun@wustl.edu

Focal adhesion kinases include focal adhesion kinase 1 (FAK, also known as FAK1 or PTK2) and the closely related protein tyrosine kinase 2 beta (PTK2β, also known as FAK2). Both are non–receptor tyrosine kinases that have been heavily studied and implicated in cancer cell migration, proliferation, and survival. Notably, they also regulate proinflammatory pathway activation and cytokine production (38–40). As such, FAK signaling has been shown to be important in wound healing and pathologic fibrosis in various tissues (41, 42). FAK signaling is hyperactivated in many cancers, including PDAC, and has been correlated with poor survival (43–44). Our group and others have shown that FAK signaling is an integral driver of the fibrotic and immunosuppressive microenvironment that protects PDAC from immune surveillance and drives resistance to immunotherapy (45–47). In this study, we address the role of stromal-induced RT resistance in immune priming. We show that FAK inhibition can sensitize PDAC to RT and promote both RT-induced immune priming and response to immunotherapy.

## RESULTS

### Radiotherapy Is Insufficient to Optimally Prime Robust T-cell Responses in PDAC

To study the effect of RT on T-cell infiltration, we first performed IHC on human surgical resection samples from patients who received neoadjuvant chemotherapy in combination with stereotactic body RT (chemo/SBRT) or with conventional RT (chemo/RT), or no neoadjuvant therapy. Across these cohorts, we found no difference in the number of tumor-infiltrating CD8+ T cells (Fig. 1A; Supplementary Table S1). Even though we did not see T-cell changes, we found the total number of CK19+ tumor cells was reduced in the tumor bed of samples from chemo/SBRT-treated patients (Supplementary Fig. S1A). In contrast, we observed increased stromal area and collagen deposition in patients who received neoadjuvant RT (Fig. 1B). These data raise the possibility that although RT can lead to temporary disease control in patients with PDAC (48, 49), it may fail to optimally prime antitumor T-cell immunity and thus limit long-term benefits. However, due to the heterogeneity of PDAC tumors and patients, these human studies in unmatched patient populations cannot fully answer this question, and larger studies with paired samples would be needed to fully address this.

To better understand whether RT can directly affect antitumor immunity in PDAC, we utilized the *p48-Cre/LSL-Kras*$^{G12D}$/*Trp53*$^{Flox/Flox}$ (KPC) genetically engineered mouse model (GEMM). The KPC tumors replicate the treatment-resistant nature and abundant stroma of human PDAC (50). Studies on the impact of RT on PDAC TME in preclinical models are limited by the lack of methods to precisely deliver targeted RT doses into the pancreata of mice. To overcome this, we used a small animal radiation research platform (SARRP; ref. 51), which incorporates computed tomography (CT) image-guided delivery of high doses of radiation (Supplementary Fig. S1B). With this instrument, we can safely deliver clinically relevant doses of radiation to the mouse pancreas while limiting off-target delivery to surrounding normal tissues. KPC mice with ultrasound-diagnosed tumors were treated with hypofractionated RT (6 Gy × 5) and monitored for tumor progression (Fig. 1C). We found RT could only modestly control tumor growth as measured by

longitudinal ultrasound imaging or tumor weights at days 7 and 14 after RT start (Fig. 1D and E; Supplementary Fig. S1C–S1E). After modest disease control, all KPC mice treated with RT eventually rapidly progressed, which was translated into no benefit in overall long-term survival (Fig. 1F). These data agree with other studies showing that, unlike transplantable tumors, these highly fibrotic KPC GEMMs exhibited limited RT response (52, 53). To understand if induction of DNA damage was impaired, we analyzed γH2Ax+ foci formation. As expected, at 6 and 24 hours after completion of hypofractionated RT, significant γH2Ax+ foci were observed in most PDAC cells and stroma, but 48 hours after the last RT dose, most γH2Ax+ foci resolved, suggesting DNA repair was intact in this model (Fig. 1G). Analysis of cleaved caspase-3+ (CC3+) cells found no induction of apoptosis at 7 or 14 days after RT start. Surprisingly, we also observed no change in the number of Ki-67+ proliferating cells on day 7, but by day 14, tumor proliferation in RT-treated tumors was elevated compared with controls (Fig. 1H; Supplementary Fig. S1F). Together, these data show that RT had limited efficacy in killing PDAC cells in stroma-rich KPC GEMMs.

Next, we sought to determine if RT could prime T-cell immunity in KPC GEMMs. We found that RT did not lead to increased PDAC-infiltrating CD8+ or CD4+ T-cell numbers (Fig. 1I; Supplementary Fig. S1G). We also did not observe any increase in the number of Ki-67+ CD8+ T cells but found the CD44+ CD62L− activated T-cell fraction was slightly decreased. These data were consistent across the 7- and 14-day post-RT time points (Fig. 1I; Supplementary Fig. S1G). Although there were no major changes in myeloid cell populations, we noted a trend toward increased monocytes, tumor-associated macrophages (TAM), granulocytes, and eosinophils at both days 7 and 14 post-RT start (Supplementary Fig. S1H). To eliminate the possibility that RT did not prime new T-cell responses because of the low neoantigen burden characteristic of KPC GEMMs, we studied RT's ability to induce tumor-specific T-cell responses in *p48-Cre/LSL-Kras*$^{G12D}$/*Trp53*$^{Flox/Flox}$/*LSL-OVA-GFP*$^+$ (KPC-OG) PDAC GEMMs (54). KPC-OG mice harbor inducible neoantigens, ovalbumin (OVA) and GFP expression, which allow for the tracking of tumor antigen–specific T cells. Despite neoantigen expression in KPC-OG mice, we found that RT did not lead to an increase in either total or OVA-specific (Dextramer+) CD8+ T cells in PDAC tissues 14 days after treatment start. In keeping with the lack of immune priming effects of RT in this model, we also observed no increase in OVA-specific Dextramer+ T cells in the pancreas draining lymph nodes (Fig. 1J). Furthermore, we found no change in the proximity of CD8+ T cells relative to CK19+ tumor cells in mice treated with RT (Supplementary Fig. S1I).

To contrast with these KPC-OG GEMMs, we used littermate mice to evaluate RT-induced T-cell immunity in sarcoma tumors. These *LSL-Kras*$^{G12D}$/*Trp53*$^{Flox/Flox}$/*LSL-OVA-GFP*$^+$ mice (called KPS-OG hereafter) were injected with Adenovirus-Cre into the hind-leg muscle to generate sarcoma tumors (55). In contrast to KPC-OG littermates, KPS-OG mice treated with the same RT regimen (6 Gy × 5) had a sustained reduction of tumor progression, decreased Ki-67+ proliferating tumor cells, and increased tumor-infiltrating CD8+ T cells as well as increased OVA-specific T cells in both the tumor tissues and draining lymph nodes (Fig. 1K; Supplementary Fig. S1J and S1K). Taken
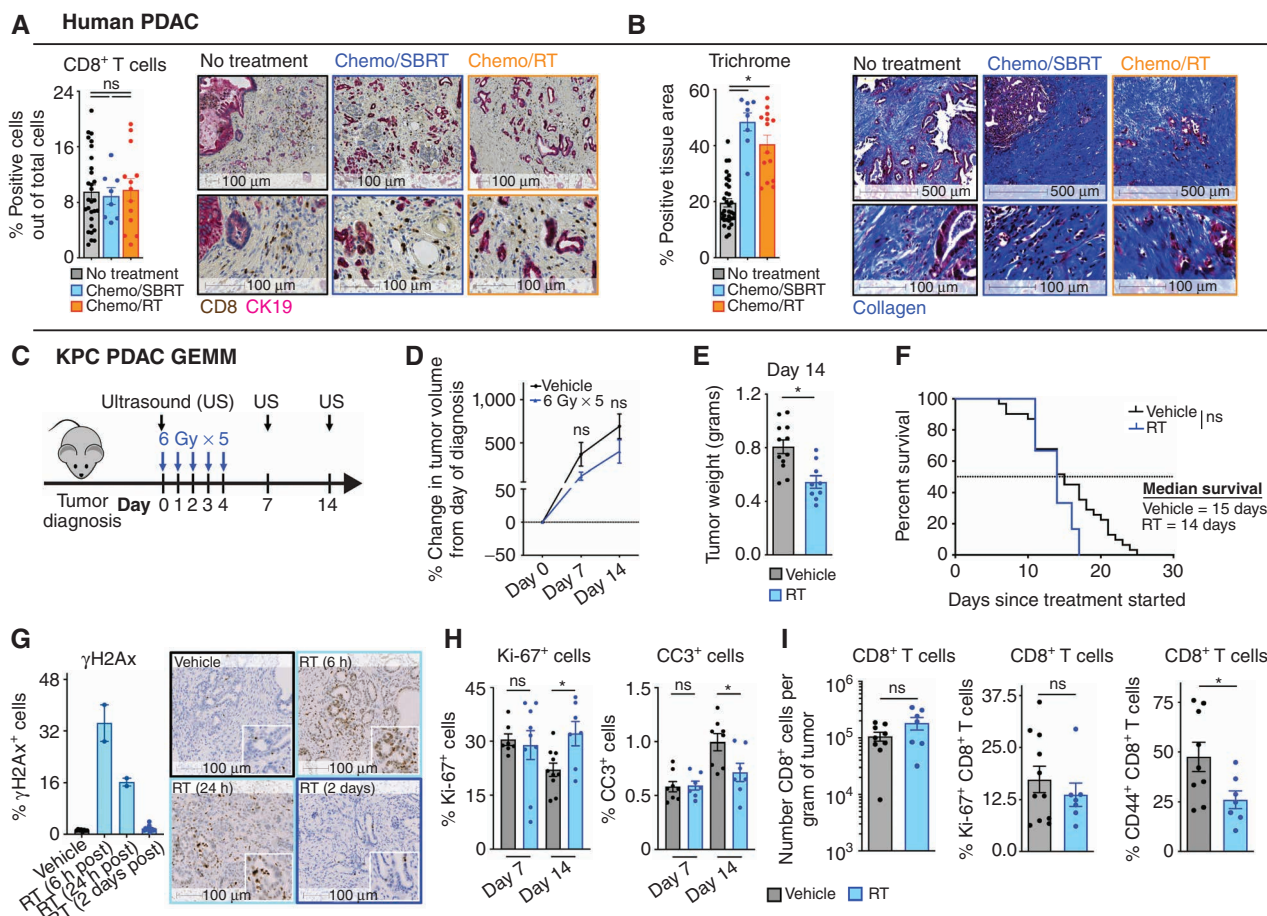
**Figure 1.** Radiotherapy is insufficient to optimally prime robust T-cell responses in PDAC. **A** and **B,** Analysis of CD8α T-cell number and collagen density in surgical resection samples from patients who received neoadjuvant chemo/SBRT, chemo/RT, or no neoadjuvant therapy. Representative CD8α/CK19 IHC and Trichrome images and quantification are depicted. $n = 8–32$ patients/group. **C,** Schematic of RT administration and tumor burden monitoring in KPC GEMMs. KPC mice diagnosed with ultrasound (US) were treated with hypofractionated RT (6 Gy × 5) and longitudinally assessed for tumor burden. **D,** Tumor growth kinetics of vehicle and RT-treated KPC mice from **C** quantified by US measurements. $n = 8–12$ mice/group. **E,** Day 14 pancreas weight of KPC mice from **C**. $n = 9–13$ mice/group. **F,** Kaplan–Meier survival curve of KPC mice from **C**. $n = 6–31$ mice/group. **G,** Analysis of DNA damage (γH2Ax) on tissues from KPC vehicle or RT-treated mice at various time points. Representative γH2Ax IHC images are depicted. $n = 2–10$ mice/group. **H,** IHC analysis of proliferation (Ki-67) and apoptosis (CC3) on tissues from KPC mice at days 7 and 14 after RT. $n =$ at least 7 mice/group. **I,** Flow cytometry quantification of total CD8+ T cells and percentage of Ki-67+ or CD44+ CD8+ T cells out of total CD8+ T cells in KPC vehicle or RT-treated mice at day 14. $n =$ at least 7 mice/group. (*continued on next page*)

together, these data suggest that in genetically equivalent mice, RT increased antigen-specific T cells in sarcoma GEMMs but failed to prime tumor immunity in PDAC GEMMs. Although both models were driven by *KRAS* mutation and *Trp53* loss, one key difference we noted was that the KPC-OG PDAC tissues had higher stromal desmoplasia compared with their KPS-OG sarcoma counterparts (Fig. 1J and K; Supplementary Fig. S1L). These data suggest that the effects of RT on tumor control and T-cell priming might be related to stromal differences.

## Stromal Elements Repress RT Efficacy and Induction of Interferons

PDAC tumors are often characterized by dramatic desmoplastic stroma comprised of dense extracellular collagen deposition and diverse CAF populations (56, 57). To test the role of PDAC stroma in RT-induced cell death, we used heterotypic organoid cell culture models. These models allow

for the coculture of PDAC organoids with fibroblasts and ECM components. PDAC organoids (KPOG) were derived from KPC-OG mice, and growth was tracked by GFP fluorescence (Fig. 2A). We found that whereas PDAC organoids alone were sensitive to RT, the addition of pancreas-derived fibroblasts rendered tumor cells less sensitive to RT, and the heterotypic organoid cocultures rapidly grew after RT exposure (Fig. 2A). Similarly, increasing collagen I density in this culture system also conferred resistance to RT (Supplementary Fig. S2A–S2C). The presence of both pancreatic fibroblasts and collagen I additively protected PDAC organoids from RT-induced growth inhibition (Fig. 2B; Supplementary Fig. S2B and S2C). To confirm this further, we used FACS to sort PDAC CAFs from KPC tumors and again observed that CAFs and collagen I worked cooperatively to protect PDAC cells from RT (Supplementary Fig. S2D). To understand how the PDAC stroma affects RT efficacy, we looked at markers of
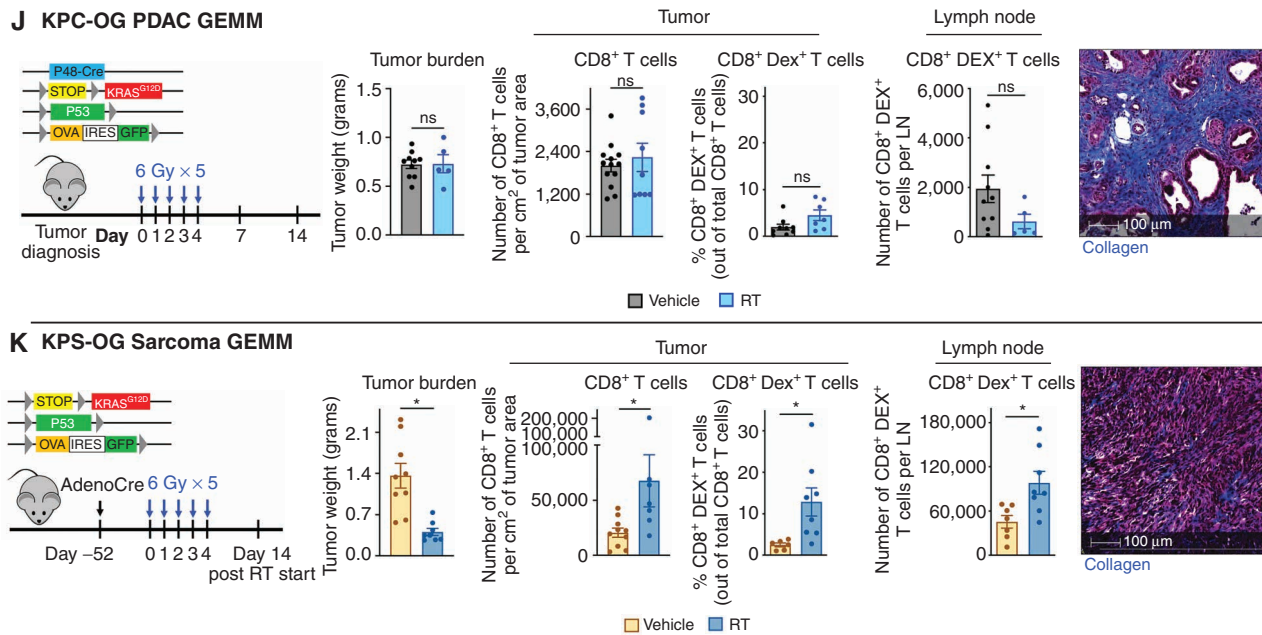
**Figure 1.** *(Continued)* **J,** Genetic loci for KPC-OG PDAC GEMMs and schematic of RT administration. Pancreas weight of KPC-OG vehicle or RT-treated mice. IHC analysis of CD8α T-cell number from KPC-OG vehicle or RT-treated mice. Flow cytometry quantification of total CD8⁺ OVA-Dextramer⁺ tumor-specific T cells from tumor and pancreas draining lymph nodes (LN) in KPC-OG vehicle or RT-treated mice. A representative Trichrome image from KPC-OG vehicle-treated mice is depicted. All analyses were done on day 14 after RT start. *n* = at least 6 mice/group. **K,** Genetic loci for KPS-OG sarcoma GEMMs and schematic of AdenoCre injection and RT administration. Tumor weight of KPS-OG vehicle or RT-treated mice. IHC analysis of CD8α T-cell number from KPS-OG vehicle or RT-treated mice. Flow cytometry quantification of total CD8⁺ OVA-Dextramer⁺ tumor-specific T cells from tumor and draining lymph nodes in KPS-OG vehicle or RT-treated mice. A representative Trichrome image from KPS-OG vehicle–treated mice is depicted. All analyses were done on day 14 after RT start. *n* = at least 7 mice/group. All graphs depict mean ± SEM. For comparisons between two groups, *, *P* < 0.05 by two-tailed *t* test, one-way ANOVA, or Kaplan–Meier as appropriate. ns, not significant.
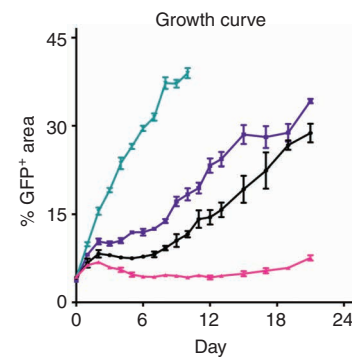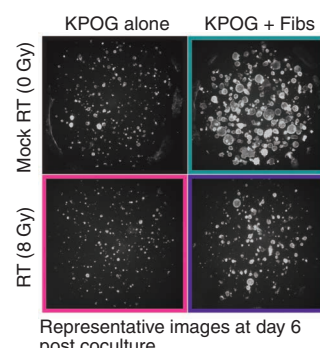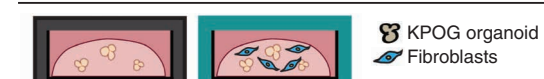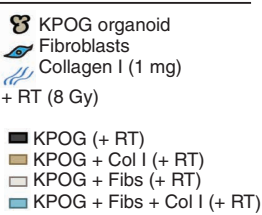
proliferation, apoptosis, and DNA damage using IHC. First, we found the induction of γH2Ax measured 6 hours post-RT was identical in the presence or absence of fibroblasts, suggesting that DNA damage induction by RT was not affected, at least in the short term (Fig. 2C). Similarly, pancreatic fibroblasts did not affect the induction of apoptosis, measured by CC3 at 3 days following RT (Fig. 2D). However, regardless of RT, fibroblasts did significantly increase the number of PDAC cells that entered S-phase after coculture, as measured by BrdUrd incorporation (Fig. 2E). These data suggest that even though RT could induce apoptosis in some cells, RT was not able to fully blunt proliferation in the presence of PDAC stroma.

To understand if there are potential changes in RT-regulated immune signaling due to the collagen-rich stroma, we measured the expression of IFN-related genes. We found that when organoids were cultured in basement membrane extract alone, robust increases in IFN-related gene expression were observed 24 to 48 hours after RT (Fig. 2F; Supplementary Fig. S2E). This included increases in genes encoding IFNα, IFNβ, IFNγ, IRF3, IRF7, IRF9, STAT1, CXCL9, CXCL10, and CXCL11 proteins. However, when collagen was added to these cultures, the induction of IFN-related genes was severely dampened (Fig. 2F; Supplementary Fig. S2E). Other inflammatory genes such as IL1α were not altered, suggesting some specificity for IFN signaling (Fig. 2F). These data suggest that stromal elements may limit not only RT-induced growth suppression, as shown by others (58–60), but also RT-induced IFN signaling, which may relate to RT-induced tumor immunity *in vivo*.
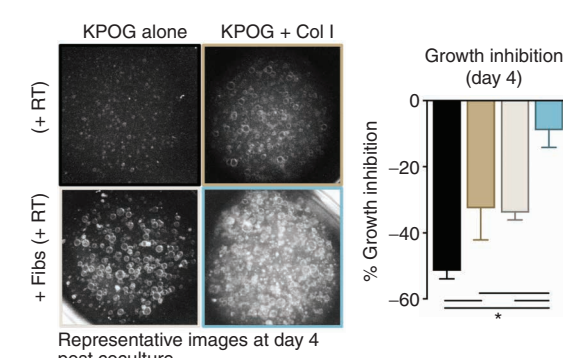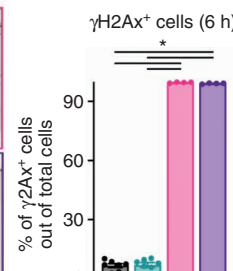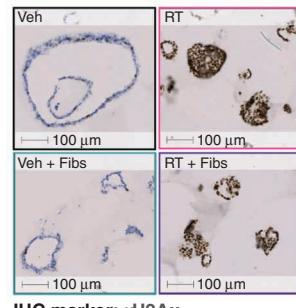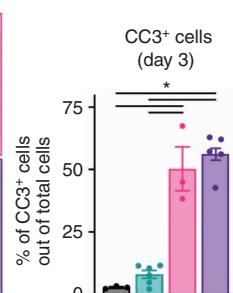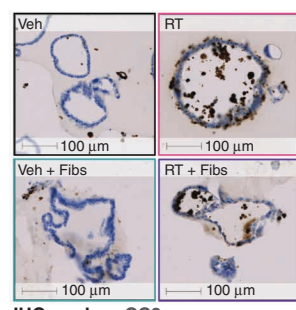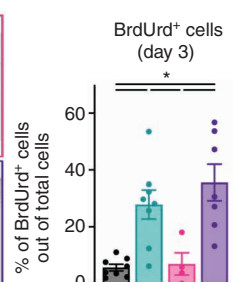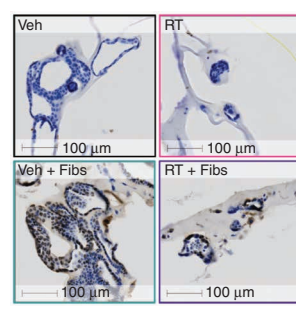
To determine if RT alone changes how PDAC cells interact with the TME, we performed RNA sequencing (RNA-seq) and reverse phase protein array (RPPA) to look at both the gene and protein levels, respectively, after RT. As expected, compared with vehicle-treated cells, RT-treated cells had higher expression of DNA damage and repair proteins, such as γH2Ax, ATM, RAD17, and RAD51 (Supplementary Fig. S2F), and increases in gene sets related to DNA damage,
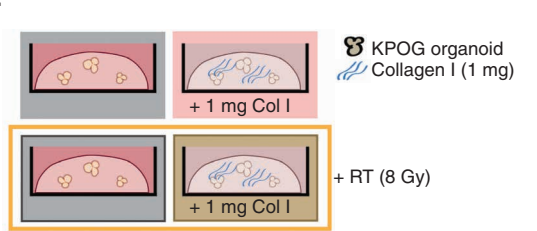
**Figure 2.** Stromal elements repress RT efficacy and induction of interferons. **A,** Experimental schematic of KPOG organoids cocultured with fibroblasts (Fibs). Cells were cultured for 1 day before RT. Representative GFP images were taken with a fluorescent microscope at day 6 after coculture. Tumor growth analysis of KPOG organoids tracked over time. *n* = at least 3/group. **B,** Experimental schematic of KPOG organoids cocultured with fibroblasts and collagen I. Cells were cultured for 1 day before RT. Representative fluorescent images and quantification of tumor growth inhibition at day 4. *n* = at least 3/group. **C,** IHC analysis and representative images of γH2Ax in KPOG organoid cultures at 6 hours after RT. *n* = at least 3 sets/group. **D** and **E,** IHC analysis and representative images of CC3 (**D**) and 5hr-pulsed BrdUrd (**E**) in KPOG organoid cultures at day 3 after RT. *n* = at least 3/group. **F,** Experimental schematic of KPOG organoids cocultured with collagen I. RT-PCR measurements of IFN-related genes were measured in KPOG organoid cultures treated with different conditions at the indicated time points. *n* = at least 3/group. All graphs depict mean ± SEM. *, *P* < 0.05 by two-tailed *t* test or one-way ANOVA as appropriate. ns, not significant.

**A** **KPOG organoid *in vitro* culture system**

**B**
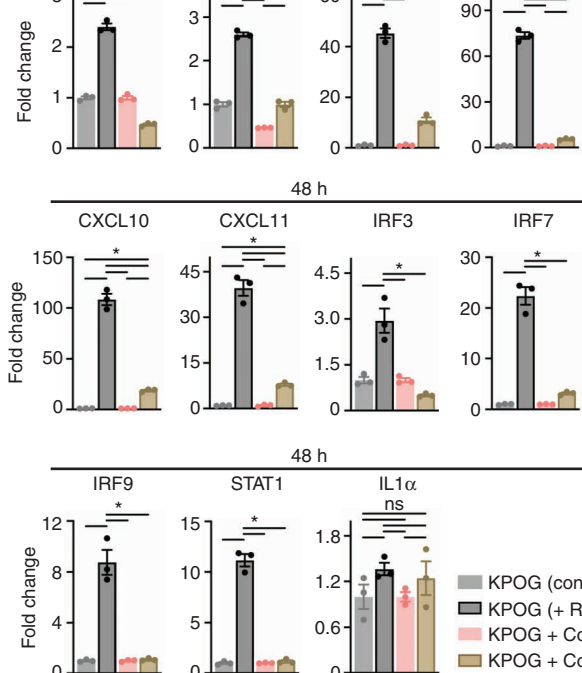
reactive oxygen species (ROS), and DNA repair (Supplementary Fig. S2G). However, RT also induced collagen, integrin signaling, and focal adhesion assembly gene signatures (Supplementary Fig. S2G). Together, these data suggest that RT might also "prime" PDAC cells to engage with the surrounding stroma through integrin and focal adhesion signaling.

## Inhibition of FAK Overcomes Stromal-Induced RT Resistance

Although seldom mutated, FAK is hyperactivated in >80% of PDAC tumors and plays an integral role in disease progression (44, 46). Furthermore, FAK signaling is amplified by stromal density and can be critical to ECM/integrin-induced survival signaling (44, 46). To understand whether we can overcome stromal-mediated RT resistance through FAK inhibition, we tested RT in combination with a FAK inhibitor (FAKi), VS-4718. As above, the presence of fibroblasts and collagen enhanced the growth of PDAC organoids and made them much less responsive to RT (Fig. 3A–C). However, the combination of FAKi and RT led to complete inhibition of PDAC organoid growth, in a FAKi dose–dependent manner (Fig. 3B-C). This was true whether PDAC cells were grown in the presence of CAFs, collagen, or both (Fig. 3C; Supplementary Fig. S3A–S3D). These findings show that FAKi can be a potential radiosensitizer for PDAC and that FAKi may increase RT efficacy.

To elucidate the effects of adding FAKi to RT, we again looked at markers of proliferation, apoptosis, and DNA damage using IHC. We did not see a difference in the short-term induction of DNA damage as measured by γH2Ax between RT and RT + FAKi in the presence or absence of fibroblasts, suggesting that neither FAK inhibition nor the presence of stroma regulated the amount of initial (first 6 hours) DNA damage induced by RT in PDAC cells (Fig. 3D). Next, we found that the combination of RT + FAKi dramatically increased the number of CC3+ apoptotic cells and decreased the number of Ki-67+ proliferating cells by 3 days post-treatment, and these effects were irrespective of the presence of stroma (Fig. 3D). These data suggest that FAK inhibition can improve RT-induced cell death.

To further understand if the cell death induced by the combination of FAKi and RT would have an immunomodulatory effect, we performed parallel RNA-seq and RPPA in KPOG organoids and the KP2 and KRAS-INK (KI) PDAC cell lines. We found PDAC cells treated with either RT or RT + FAKi had significant upregulation of DNA damage response gene sets and proteins, including DNA damage and ROS-related genes and AMPK, pERK, DNA Ligase-IV, TIGAR, and RAD17 proteins (Fig. 3E; Supplementary Fig. S3E). However, unlike RT-treated cells, RT + FAKi-treated cells had downregulation of gene sets related to DNA damage repair and ROS response, as well as downregulation of key DNA damage repair signaling proteins (NQO1, JAB1, KEAP1, RAD23, and DDB1; Fig. 3E; Supplementary Fig. S3E). As expected, RT + FAKi-treated cells also had changes in cell-cycle gene sets and cell-cycle proteins (CDK1, p27, CDC2, CyclinD3, and CDK9) corresponding to the observed changes in growth arrest (Fig. 3E and F; Supplementary Fig. S3E). Finally, we observed that RT + FAKi treatment might change key metabolic pathways, including downregulation in genes related to oxidative phosphorylation, glycolysis, cholesterol homeostasis, and DNA

replication (Fig. 3E–G; Supplementary Fig. S3E). However, whether these metabolic changes were associated with unique biology or just cell-cycle arrest and death is unclear. Taken together, these suggest that although both RT and RT + FAKi can induce DNA damage response, only RT + FAKi inhibits the ability of PDAC cells to repair damage, leading to growth arrest.

Next, we examined the expression of key proliferative signaling mediators for PDAC cells and observed that RT + FAKi led to the downregulation of numerous MAPK proteins and prosurvival/apoptosis-related proteins, including MEK2, ERK5, p38, PLCγ, NOTCH1, AKT, XIAP, and PARP, and upregulation of mTOR/autophagy-related proteins ATG7, p70-S6K1, mTOR pS2448, Rictor, S6, and ULK1 (Fig. 3E; Supplementary Fig. S3E). Notably, some of these changes were also seen with FAKi monotherapy, suggesting that inhibition of FAK drives these changes in our system.

To understand the potential immunologic impact of RT + FAKi treatment, we analyzed changes in the inflammatory pathways in PDAC cells and organoids. By RNA-seq, we observed upregulation of gene sets involved in TNFα, IFNβ, and IFNγ signaling (Fig. 3F–H). Additionally, RT + FAKi-treated PDAC cells had increased expression levels of genes related to antigen processing and presentation (Fig. 3G and H), possibly downstream of increased IFN signaling. Correspondingly, increases in NFκB, JNK, and c-JUN pathways were observed at the protein level with RT + FAKi treatment, whereas STAT3 and JAK2 protein expressions were decreased (Fig. 3E; Supplementary Fig. S3E). Using orthogonal approaches, we found that STING and phospho-IRF3 were increased by Western blot analysis and IFNα, IFNβ, and IFNγ transcripts were upregulated by RT-PCR in KI cells treated with RT + FAKi (Supplementary Fig. S3F–S3G). To confirm the observed changes in STAT/IFN signaling in vivo, we performed multiplex IHC (mIHC) on PDAC tissues from KPC mice and found that RT + FAKi treatment elevated phospho-STAT1 (pSTAT1) expression in CK19+ PDAC cells (Fig. 3I). Taken together, these data suggest that FAK inhibition overcomes stromal-induced RT resistance by mitigating prosurvival and DNA damage repair signaling, which ultimately leads to sustained activation of IFN pathways in PDAC cells.

## Combining FAKi with RT Leads to Immune Priming In Vivo

We next sought to determine if FAK inhibition could improve RT efficacy and immune priming in vivo. To accomplish this, we treated KPC GEMMs with the combination of RT and FAKi (Fig. 4A). Longitudinal ultrasound imaging showed that RT + FAKi led to dramatic PDAC tumor regression in nearly 100% of mice (Fig. 4B and C). These imaging data were verified by absolute pancreas weights from mice sacrificed 7 and 14 days after RT start (Fig. 4D; Supplementary Fig. S4A). Additionally, RT + FAKi led to superior tumor regression than the combination of RT with the chemotherapeutic drug gemcitabine, which has been used to treat patients with PDAC (Fig. 4B and C). Similarly, RT + FAKi led to tumor regression and long-term survival in multiple PDAC models representing diverse tumor suppressor alterations, including KPC and KPC-OG GEMMs, syngeneic KP2 (Kras^G12D/Trp53^Flox/+), PDA.69 (Kras^G12D/Trp53^R172H/+), and KI (Kras^G12D/Trp53^+/+/Ink/Arf^Flox/Flox;
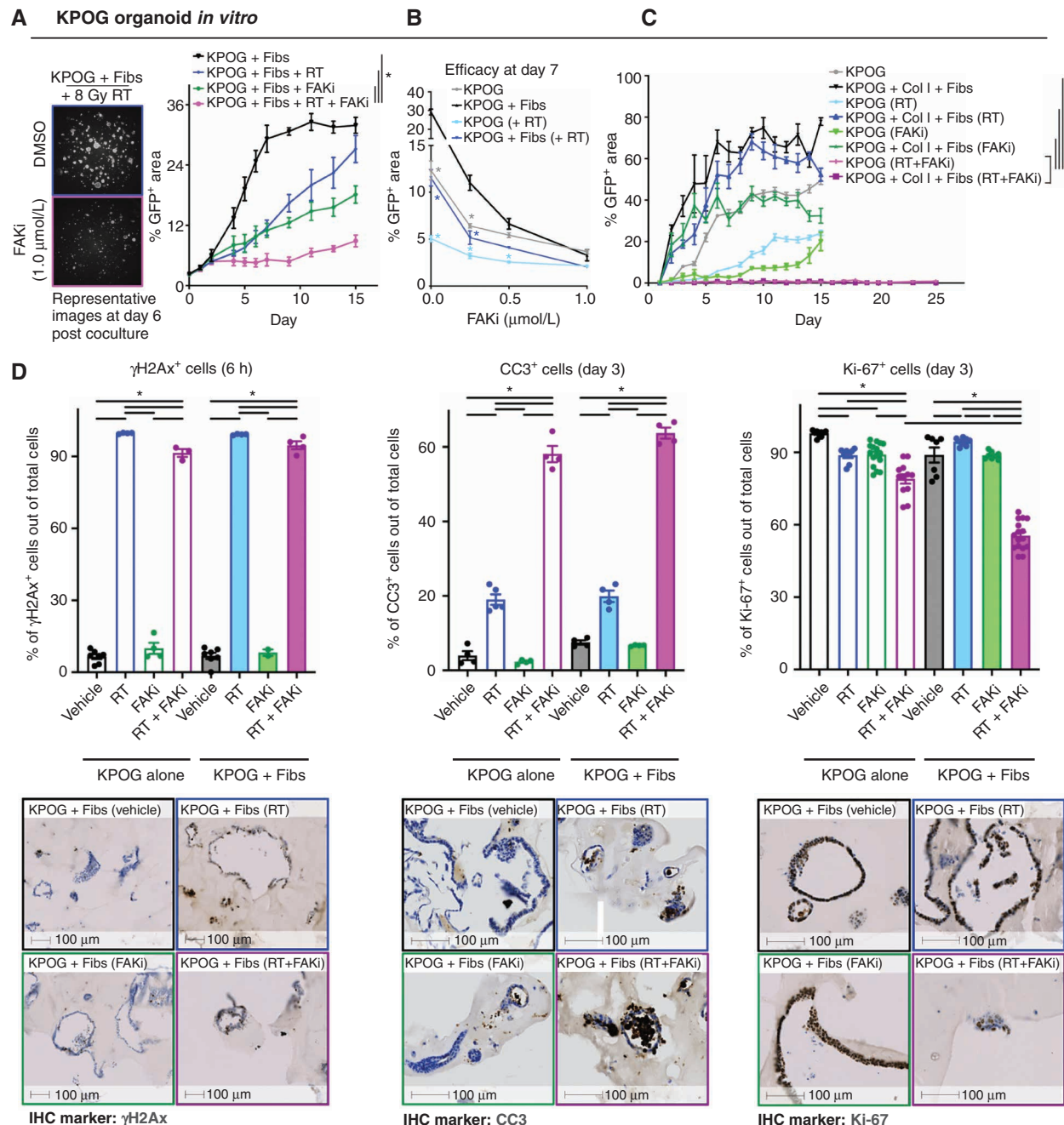
**Figure 3.** Inhibition of FAK overcomes stromal-induced RT resistance. **A,** Tumor growth analysis of KPOG organoids cocultured with fibroblasts (Fibs) treated with RT ± FAKi. Cells were cultured as in Fig. 2A. Representative fluorescent images at day 6 after coculture. $n$ = at least 3/group. **B,** Growth analysis of KPOG organoids cocultured with fibroblasts after treatment with RT ± FAKi at varying concentrations at day 7 after coculture. $n$ = at least 3/group. **C,** Tumor growth analysis of KPOG organoids cocultured with fibroblasts and collagen I treated with RT ± FAKi. $n$ = at least 3/group. **D,** IHC analysis of γH2Ax in KPOG organoid cultures taken 6 hours after RT. IHC analysis of CC3 and Ki-67 in KPOG organoid cultures taken 3 days after RT. Representative γH2Ax, CC3, and Ki-67 IHC images are depicted. $n$ = at least 3/group. (continued on next page)

Fig. 4E and F; Supplementary Fig. S4A–S4D). Corresponding with the observed efficacy, in KPC GEMMs, RT + FAKi markedly reduced cell proliferation (Ki-67+ cells), CK19+ tumor cells, and high-grade PDAC lesions and increased the number of CC3+ apoptotic cells, necrotic tumor, and normal pancreatic tissue areas, compared with tissues from mice treated with RT alone (Fig. 4G and H; Supplementary Fig. S4E and S4F).

Together, these data suggest RT + FAKi led to improved PDAC cell killing *in vivo*.

To determine if the observed efficacy of RT + FAKi was also associated with treatment-induced T-cell priming, we assessed changes in tumor antigen–specific T cells in KPC-OG GEMMs. Analysis of these mice at 14 days after dual RT + FAKi treatment demonstrated increases in CD8+
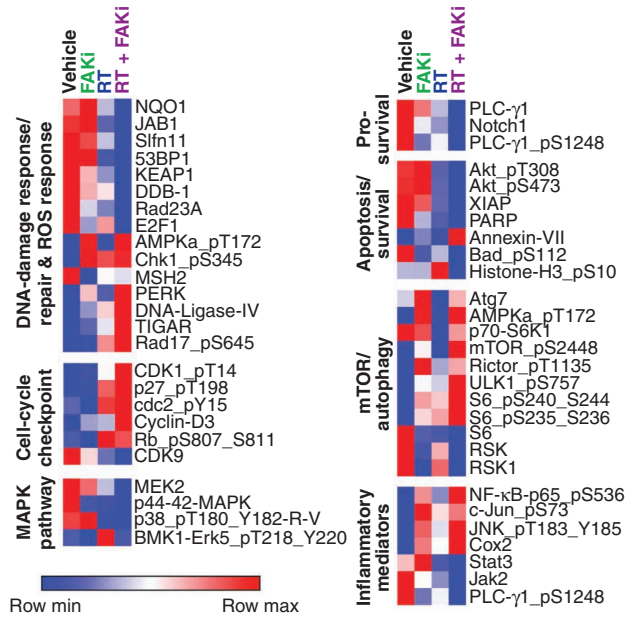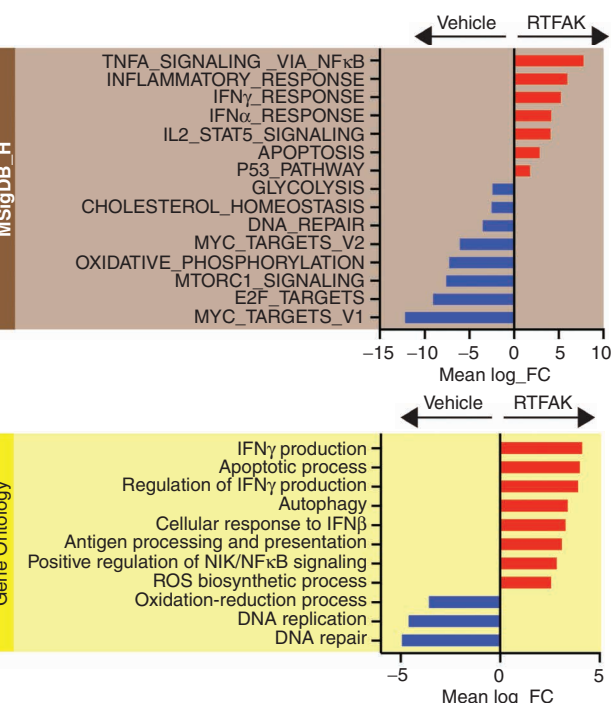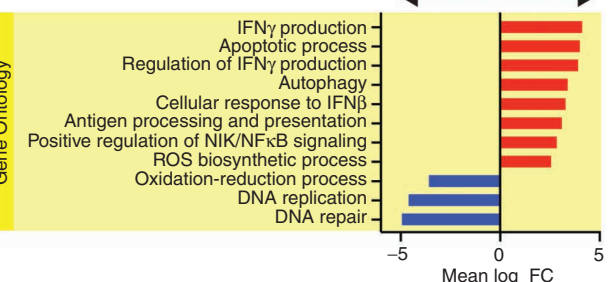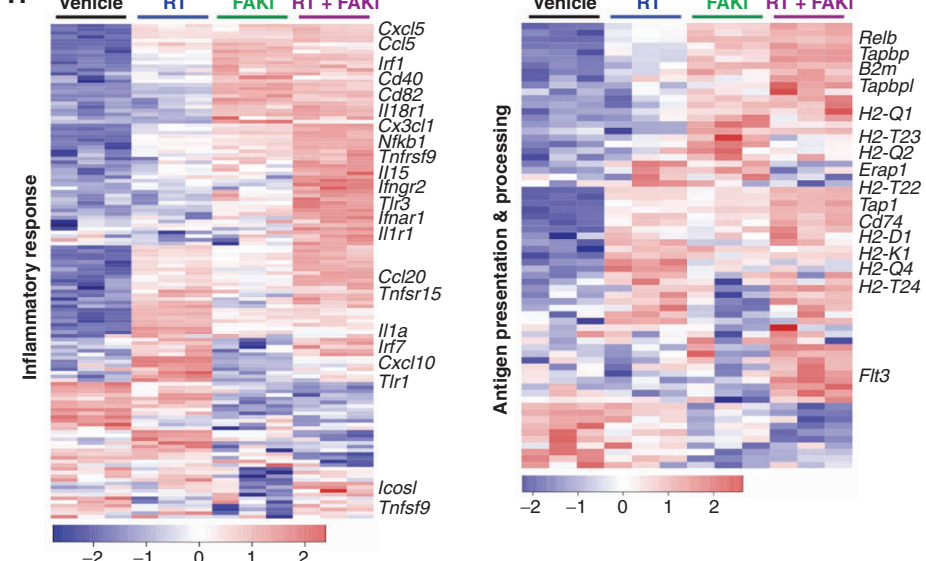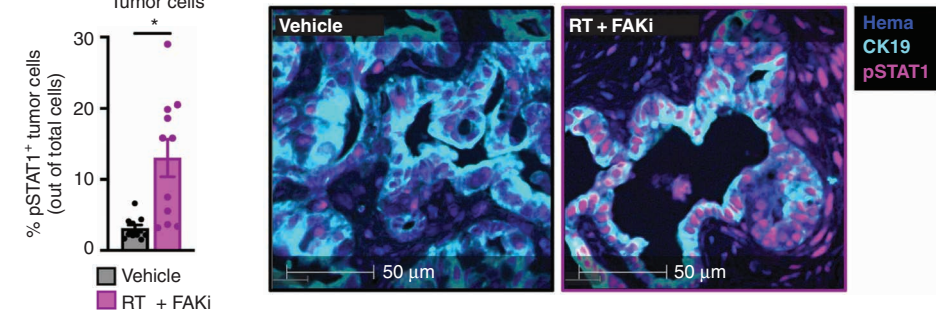
**E** Proteomics (KP2)



**F**



**G**



**H**



**I**



**Figure 3.** *(Continued)* **E,** RPPA analysis heat map displaying expression level of proteins related to DNA damage response/repair and ROS response, cell-cycle checkpoint, MAPK pathway, prosurvival, apoptosis/survival, mTOR/autophagy, and inflammatory mediators. Proteins were taken from KP2 cells 24 hours after RT. *n* = at least 3/group. **F** and **G,** Bar graphs displaying over-representation analysis of KPOG organoid differentially expressed genes (DEG) in Molecular Signatures Database (MSigDB)_Hallmark (**F**) and Gene Ontology (GO; **G**) gene sets. All graphs display comparisons of vehicle to RT + FAKi-treated cells. All pathways were filtered with *P* < 0.05. **H,** Heat map displaying the expression level of genes in the MSigDB_Hallmark database for "inflammatory response" and in the GO database for "antigen processing and presentation." **I,** mIHC analysis of CK19+ pSTAT1+ cells in tissues of KPC mice from Fig. 4A. Representative CK19 and pSTAT1 fused mIHC images are depicted. *n* = at least 6 mice/group. All graphs depict mean ± SEM. *, *P* < 0.05 by two-tailed *t* test or one-way ANOVA as appropriate.
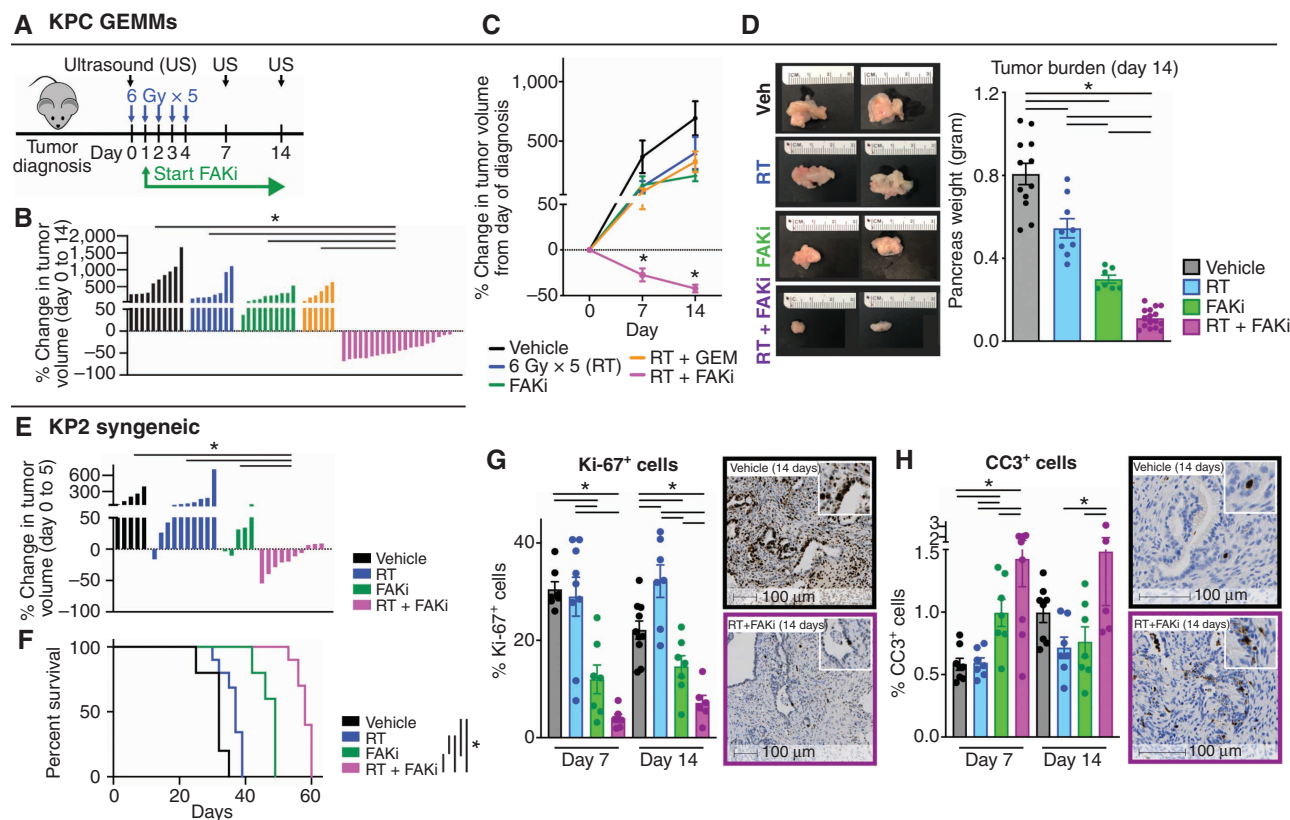
**Figure 4.** Combining FAKi with RT leads to immune priming *in vivo*. **A,** Schematic of RT (6 Gy × 5) and FAKi (75 mg/kg twice a day) administration and tumor burden monitoring in KPC GEMMs. KPC mice diagnosed with US were treated and longitudinally assessed for tumor burden. **B,** Waterfall plot of KPC GEMMs from **A** evaluating tumor growth difference from days 0 to 14 by US measurement. Gemcitabine (GEM) was given at a dose of 75 mg/kg every 5 days starting at day 0. $n = 6$–20 mice/group. **C,** Tumor growth kinetics of KPC mice from **B** quantified by US measurements. $n = 6$–20 mice/group. **D,** Day 14 pancreas weight of KPC mice from **A**. Representative gross tissue images are depicted. $n = 6$–20 mice/group. **E,** Waterfall plot of KP2 syngeneic tumor-bearing mice treated as depicted in **A** evaluating tumor growth difference from days 0 to 5. $n = 5$–10 mice/group. **F,** Kaplan–Meier survival curve of KP2 syngeneic tumor-bearing mice from **G**. $n = 5$–10 mice/group. **G** and **H,** IHC analysis of Ki-67 (**G**) and CC3 (**H**) in tissues from KPC mice at days 7 and 14 after treatment start. Representative Ki-67 and CC3 IHC images are depicted. $n =$ at least 7 mice/group. (*continued on next page*)

T-cell activation (CD44$^+$), increased number of tumor-specific OVA-Dextramer$^+$ CD8$^+$ T cells, and increased CD8$^+$ T-cell proximity to CK19$^+$ tumor cells (Fig. 4I and J; Supplementary Fig. S4G). We next analyzed draining lymph nodes from these mice and found that RT + FAKi treatment dramatically increased the total number of activated CD44$^+$ CD8$^+$ T cells and OVA-Dextramer$^+$ CD8$^+$ T cells (Fig. 4I; Supplementary Fig. S4G), suggesting RT + FAKi could lead to treatment-induced immune priming not seen with RT alone. Analysis of other immune cell populations showed that RT + FAKi decreased the total number of CD4$^+$ FOXP3$^+$ T regulatory cells, TAMs, granulocytes, and eosinophils, and increased conventional type 1 dendritic cells (cDC1) but not type 2 dendritic cells (cDC2; Fig. 4K; Supplementary Fig. S4H). In particular, the increase in cDC1, which was >13-fold, and the increase in the ratio of cDC1 to TAMs, which was >24-fold, might be directly contributing to the treatment-induced increase in tumor-specific CD8$^+$ T cells in KPC-OG GEMMs. We next sought to determine whether T cells were critical to initial tumor regression and/or improved long-term disease control. To accomplish this, we depleted CD4$^+$ and CD8$^+$ T cells in mice bearing syngeneic KP2 PDAC tumors and found that loss of T cells did not affect short-term tumor regression

(Fig. 4L; Supplementary Fig. S4I), but was critical for long-term disease control (Fig. 4M; Supplementary Fig. S4I). To determine the role of type I IFNs, we treated mice with αIFNα/β receptor 1 (αIFNAR1)–blocking antibody and observed a loss of tumor control by RT + FAKi, suggesting that IFN signaling is important for tumor control (Supplementary Fig. S4J). Altogether, these data suggest that RT + FAKi remodeled the immune TME to favor T-cell priming, and that this was critical for long-term disease control.

## Tumor-Infiltrating Immune Cells from RT + FAKi-treated Mice Have Better Antitumor Signatures

To further understand treatment-induced changes in the immune TME, we performed parallel single-cell RNA-seq (scRNA-seq) and mass cytometry (CyTOF). For scRNA-seq, we analyzed CD45$^+$ cells from the PDAC tissues of KPC GEMMs treated with vehicle, RT, FAKi, or RT + FAKi at day 14 after the start of treatment. Using uniform manifold approximation and projection (UMAP) representation, we could distinguish all major immune cell populations (Fig. 5A; Supplementary Fig. S5A). To elucidate differences in TAM phenotype, we reclustered these cells and observed five TAM clusters (termed Arg1-TAMs, Ccl7-TAMs, Apoe-TAMs, Ifitm3-TAMs,
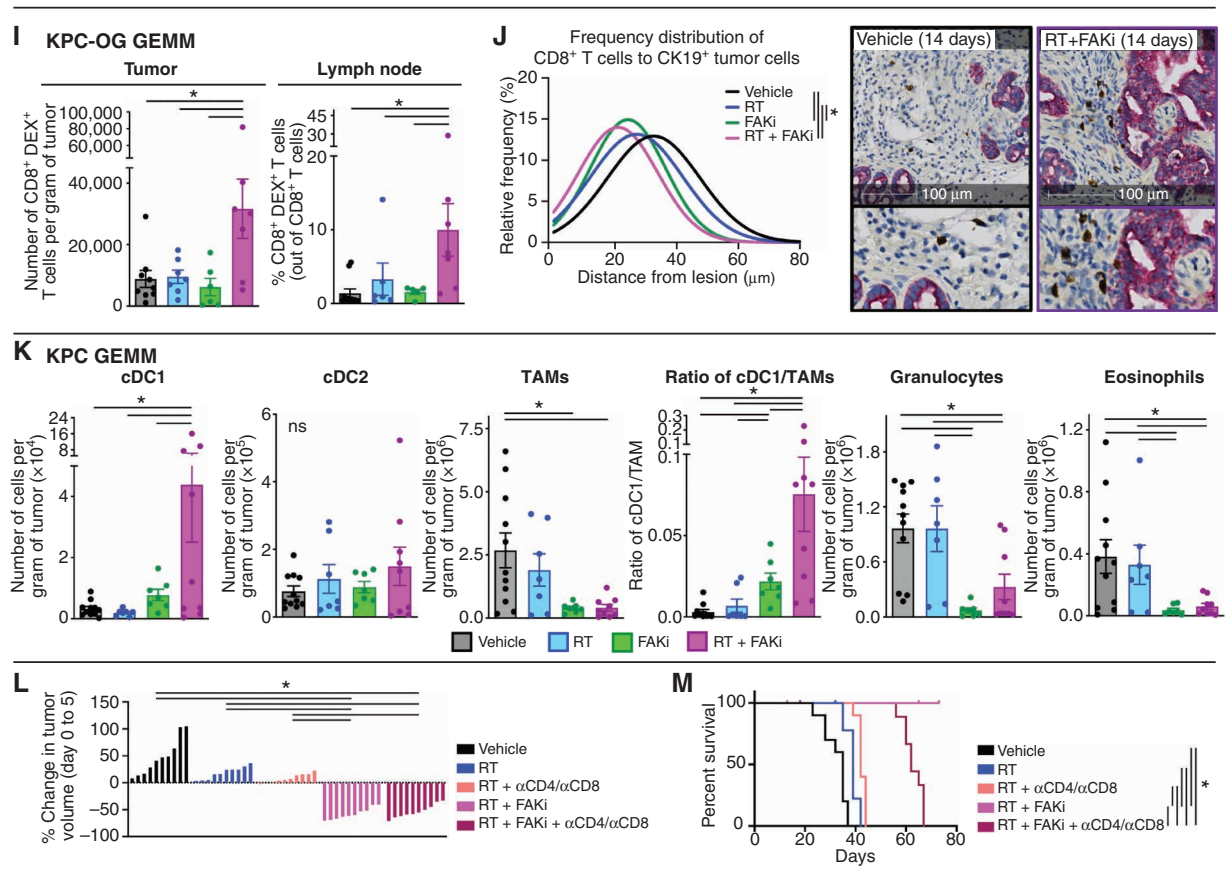
**Figure 4.** *(Continued)* **I,** Flow cytometry quantification of total CD8+ OVA-Dextramer+ T cells in tumor and pancreas draining lymph node from KPC-OG mice treated as in **A**. $n$ = at least 7 mice/group. **J,** Frequency distribution of CD8+ T-cell proximity to nearest CK19+ tumor cell in KPC-OG mice treated as indicated. Representative dual stained CD8α and CK19 images are depicted. $n$ = at least 5 mice/group. **K,** Flow cytometry quantification of various innate immune infiltrates: cDC1 (CD45+ CD3− CD19− Ly6C− Ly6G− F4/80lo MHC-IIhi CD24hi CD103+), cDC2 (CD45+ CD3− CD19− Ly6C− Ly6G− F4/80lo MHC-IIhi CD24lo CD11b+), TAMs (CD45+ CD3− CD19− Ly6C− Ly6G− CD11b+ F4/80+ MHC-II+), granulocytes (CD45+ CD3− CD19− Ly6C− Ly6G+), and eosinophils (CD45+ CD3− CD19− Ly6C− Ly6G− CD11b+ F4/80− MHC-II−) in KPC mice from **A**. $n$ = at least 7 mice/group. **L,** Waterfall plot of KP2 syngeneic tumor-bearing mice treated as in **A** evaluating tumor growth difference from day 0 to 5. Depleting αCD4 and αCD8 IgGs were given starting at day −2 every 4 days for a total of 30 days. $n$ = 10 mice/group. **M,** Kaplan–Meier survival curve of KP2 syngeneic tumor-bearing mice from **L**. $n$ = 10 mice/group. All graphs depict mean ± SEM. *, $P < 0.05$ by two-tailed $t$ test or one-way ANOVA or Kaplan–Meier as appropriate. ns, not significant.

and Ccl7-TAMs; Fig. 5B; Supplementary Fig. S5B). Among these, we observed shifts in TAM subsets in RT + FAKi-treated tumors compared with all other treatments. This included decreased frequencies of Arg1-TAMs and increased frequencies of Ifitm3-TAMs and Ccl7-TAMs (Fig. 5C), suggesting possible changes toward T-cell supportive and IFN-responsive phenotypes. To further investigate this, we performed gene set enrichment analysis (GSEA) across all TAM subsets from vehicle versus RT + FAKi-treated mice and found upregulation of pathways associated with type I and II IFNs, T-cell activation, phagocytosis, antigen processing and presentation, and ROS production (Fig. 5D and E; Supplementary Fig. S5C–S5E). In agreement with scRNA-seq, CyTOF analysis of TAMs showed increased CD80, CD86, CD11c, and PD-L2 expression and decreased VISTA in RT + FAKi-treated mice compared with RT-treated mice (Fig. 5F–G; Supplementary Fig. S5F and S5G). These data suggest that RT + FAKi treatment shifted TAMs away from immunosuppressive phenotypes and toward immune-supportive roles.

As cDCs are critical to the induction of T-cell priming, we next sought to determine how RT + FAKi altered their

phenotype. We first isolated and reclassified cDC populations and adaptive immune cells by UMAP analysis (Fig. 5H–I). In cDCs, we defined three distinct clusters: cDC1, cDC2, and migratory DC (Fig. 5H; Supplementary Fig. S5H). Mirroring our flow cytometry data (Fig. 4K), we found that PDAC tissues from RT + FAKi-treated mice had an increased frequency of cDC1s (Supplementary Fig. S5I). GSEA and overrepresentation analyses found that RT + FAKi increased expression of genes in the type I and II IFNs, TNFα, and IL12 pathways, as well as increased gene signatures for phagocytosis, antigen processing and presentation, and T-cell activation across multiple cDC populations (Fig. 5J–L; Supplementary Fig. S5J). By contrast, we observed decreases in pathways associated with DNA repair, MYC targets, oxidative phosphorylation, and MTOR signaling (Fig. 5K). Corroborating the changes in antigen presentation, we observed that RT + FAKi upregulated CD80 and CD86 in cDC1s and cDC2s, and decreased TIM3 in the cDC1s by CyTOF analysis (Fig. 5G). Together, these data suggest that cDCs were both numerically increased and phenotypically shifted toward an improved antitumor phenotype.
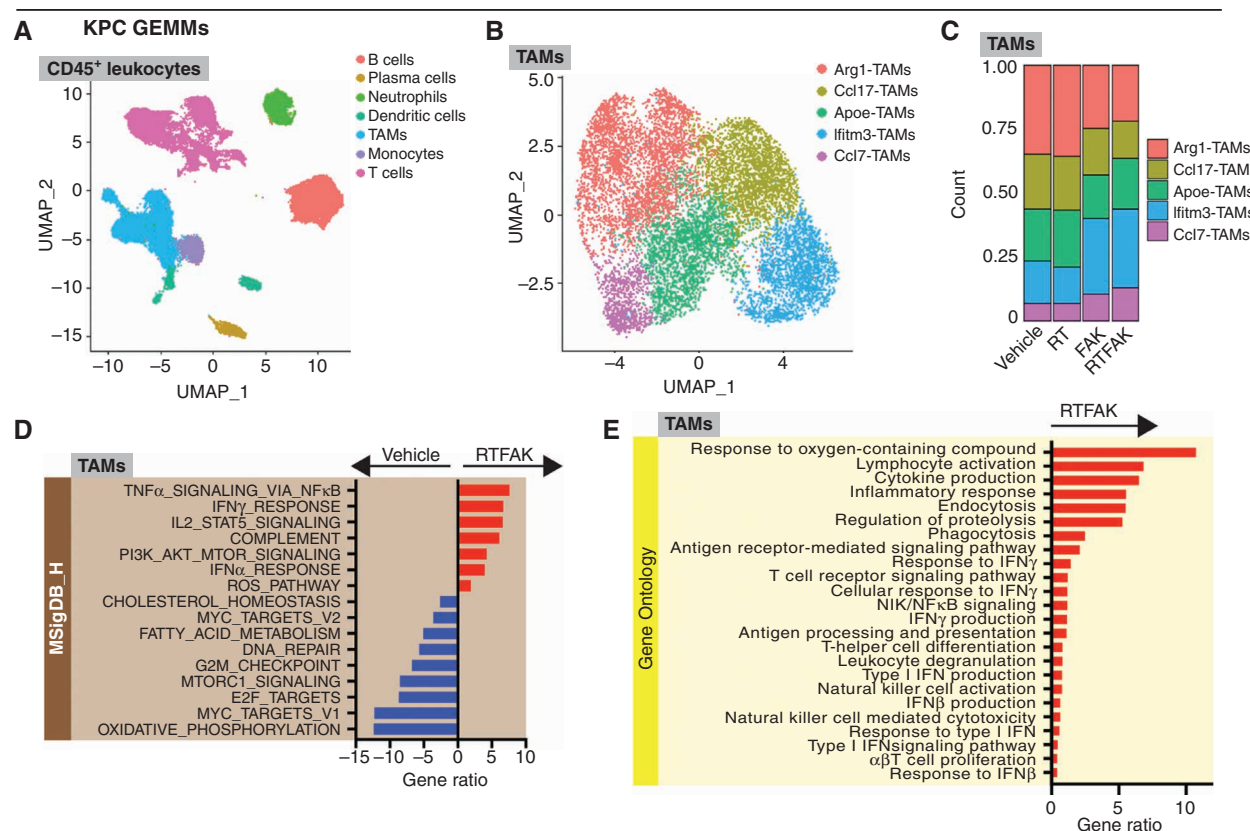
**Figure 5.** Tumor-infiltrating immune cells from RT + FAKi-treated mice have better antitumor signatures. **A,** UMAP dimensionality reduction plot of scRNA-seq data on CD45⁺ leukocytes from KPC mice at day 14 treated as depicted in Fig. 4A. Annotation shows different cell types. **B,** UMAP analysis of TAM subsets isolated from **A**. Five different TAM clusters are depicted. **C,** Count ratio of the TAM clusters from **B. D** and **E,** Bar graph displaying overrepresentation analysis of DEGs on all the TAMs in **B** to known biological functions in MSigDB_Hallmark (**D**) and GO databases (**E**). All graphs display comparisons of vehicle to RT + FAKi-treated mice. All pathways were filtered with $P_{adj} < 0.05$. (*continued on next page*)

Finally, we utilized parallel scRNA-seq and CyTOF to assess the impact these changes had on T-cell phenotype. To accomplish this, we identified CD4 and CD8 α/β T cells by UMAP analysis of the adaptive immune cells in our scRNA-seq datasets (Fig. 5I; Supplementary Fig. S5K). Agreeing with the increase in activated CD8⁺ T cells found following RT + FAKi by flow cytometry (Supplementary Fig. S4G), differential gene pathway analyses by scRNA-seq found increases in pathways involved in lymphocyte-mediated cytotoxicity, downstream antigen receptor signaling, lymphocyte activation, diversification of T-cell receptor (TCR) genes, lysosome/autophagosome, secretory/zymogen granules, and antigen and cytokine binding, as well as decreases in integrin, VEGF, FGF, and angiogenesis pathways (Fig. 5M; Supplementary Fig. S5L). A heat map displaying differential gene expression of activation/effector marker also showed that many of these genes were upregulated in the dual RT + FAKi treatment compared with vehicle or monotherapies (Supplementary Fig. S5M). CyTOF analysis of T cells defined several CD4⁺ and CD8⁺ T-cell clusters (Fig. 5N–O; Supplementary Fig. S5N and S5O). OVA-Dextramer⁺ CD8⁺ T cells were prominent in the exhausted effector (high for PD1, LAG3, and TIM3, but not for Ki-67) and the proliferative effector (high for T-bet, EOMES, and Ki-67) compartments (Fig. 5O; Supplementary Fig. S5N). We also noted that RT + FAKi-treated mice had

increased expression of activation/effector markers, such as T-bet, CD44, and OX40 in OVA-Dextramer⁺ CD8⁺ T cells, and increased frequency of Ki-67⁺ OVA-Dextramer⁺ CD8⁺ T cells compared with other treatments (Fig. 5P–Q; Supplementary Fig. S5P). However, many OVA-Dextramer⁺ T cells were in the exhausted cluster with high PD-1, LAG3, and TIM3 expression, and RT + FAKi increased the fraction of OVA-Dextramer-negative CD8⁺ T cells that clustered in the exhausted fraction (Fig. 5O and R; Supplementary Fig. S5N). These data suggest that T-cell checkpoint might be engaged during treatment. Analysis of CD4⁺ effector T cells showed increased OX40 and CD69 expression in PDAC tissue from mice treated with RT + FAKi, suggesting that, though not as dominant, CD4⁺ T cells might also play a role (Supplementary Fig. S5Q). Taken together, our data suggest that both innate and adaptive tumor-infiltrating immune cells from RT + FAKi-treated mice acquired a more antitumor phenotype; however, it is unclear if this will be confounded or aided by changes in desmoplastic stromal responses.

## FAKi Reshapes CAFs to Participate in Tumor Immunity

Like tumor-infiltrating immune cells, CAFs, which are abundant in PDAC, can play a large role in determining treatment response (12, 13, 17, 27, 29, 61). To further understand
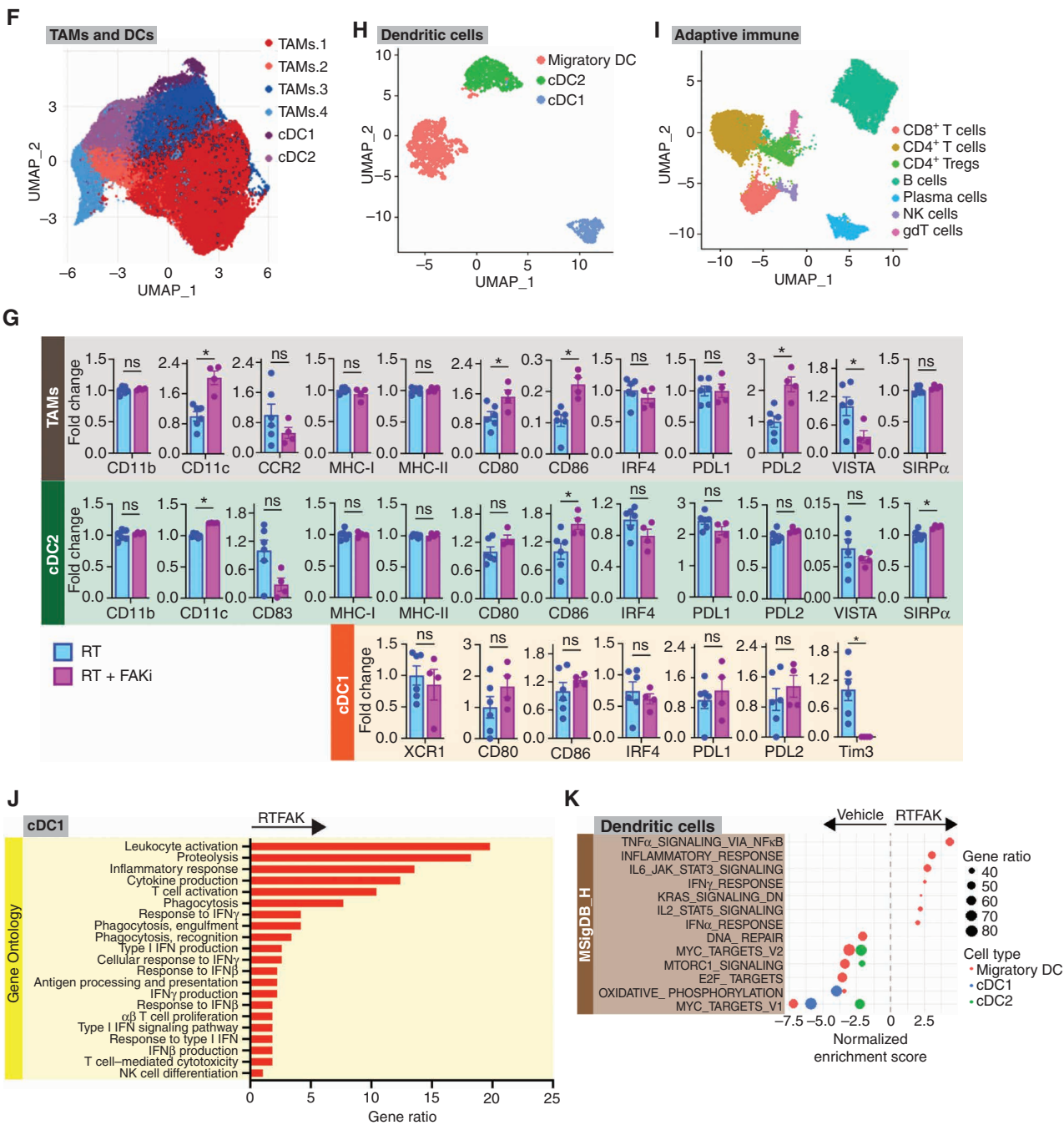
**Figure 5.** *(Continued)* **F,** UMAP dimensionality reduction plot of CyTOF data on TAMs and cDCs from KP2-OVA-GFP tumor–bearing RT and RT + FAKi-treated mice treated as depicted in Fig. 4A. Annotation shows different cell types. **G,** Analysis of median expression levels of various markers on the TAMs, cDC1, and cDC2 in **F**. $n$ = at least 4 groups of pooled mice/group. **H,** UMAP analysis of cDC subsets isolated from **A**. Three different cDC clusters are depicted. **I,** UMAP dimensionality reduction plot of scRNA-seq data on the adaptive immune cells from KPC mice. Annotation shows different cell types. **J,** Bar graph displaying overrepresentation analysis of DEGs on cDC1 to known biological functions in the GO database. All graphs display comparisons of vehicle to RT + FAKi-treated mice. All pathways were filtered with $P_{adj} < 0.05$. **K,** Dot plot displaying GSEA results from MSigDB_Hallmark database comparing different cDC clusters from **H**. All graphs display comparisons of the vehicle to RT + FAKi-treated mice. All pathways were filtered with $P_{adj} < 0.05$. *(continued on following page)*

how our treatments changed the PDAC CAFs, we performed scRNA-seq from CAF-enriched CD45⁻, CD31⁻, EPCAM⁻, PDPN⁺ cells isolated by FACS from KPC mice 14 days after treatment start. UMAP analysis of these CAFs generated seven unique subclusters (Fig. 6A; Supplementary Fig. S6A). Using known CAF markers (28, 29), we were able to identify

the classic myofibroblastic CAFs (myCAF) marked by *Acta2* and *Col12a1*, inflammatory CAFs (iCAF) marked by *Cxcl12* and *Ly6c*, and antigen-presenting CAFs (apCAF) marked by *Cd74* and *H2Ab1* (Supplementary Fig. S6A–S6C). Interestingly, treatments containing FAKi generated distinct CAF clusters that did not fall into the 3 classic CAF clusters
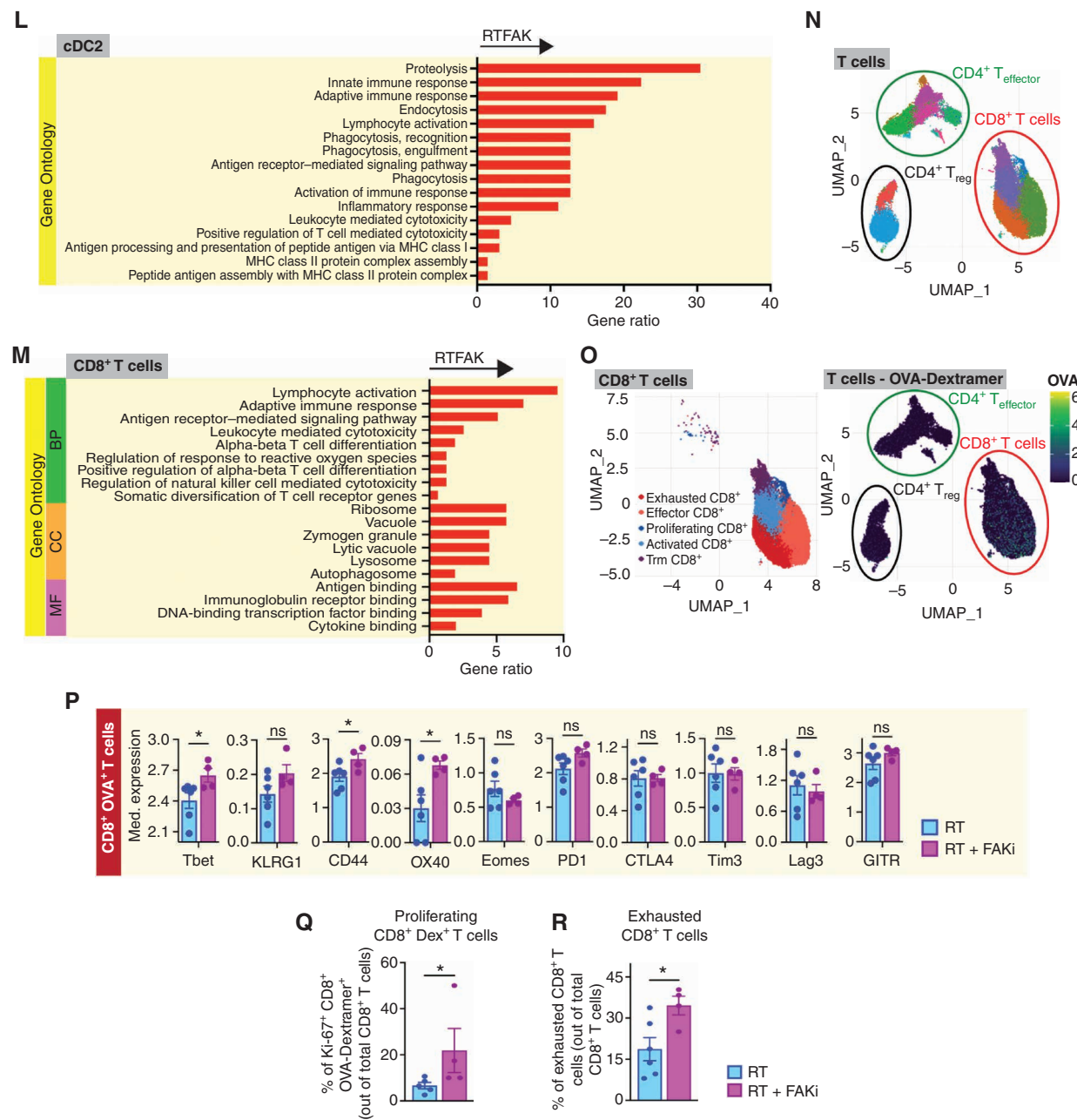
**Figure 5.** *(Continued)* **L,** Bar graph displaying overrepresentation analysis of DEGs on cDC2 to known biological functions in the GO database. All graphs display comparisons of the vehicle to RT + FAKi-treated mice. All pathways were filtered with $P_{adj} < 0.05$. **M,** Bar graph displaying overrepresentation analysis of DEGs on CD8+ T cells to known biological functions in the GO database for biological process (BP), cellular component (CC), and molecular function (MF). All graphs display comparisons of vehicle to RT + FAKi-treated mice. All pathways were filtered with $P_{adj} < 0.05$. **N,** UMAP dimensionality reduction plot of CyTOF data on CD8+ and CD4+ T-cell populations from KP2-OVA-GFP tumor–bearing RT and RT + FAKi-treated mice. Annotation shows different cell types. **O,** UMAP dimensionality reduction plot of CyTOF data on CD8+ T-cell populations from **N**. Annotation shows five different CD8+ T-cell subclusters. OVA-Dextramer expression levels projected onto UMAP plots in **N. P,** Analysis of median expression levels of various markers on CD8+ OVA-Dextramer+ T cells in **O**. *n* = at least 4 groups of pooled mice/group. **Q,** Quantification of proliferating CD8+ OVA-Dextramer+ T cells out of total CD8+ T cells from mice treated as indicated. *n* = at least 4 groups of pooled mice/group. **R,** CyTOF quantification analysis of exhausted CD8+ T cells in **N**. *n* = at least 4 groups of pooled mice/group. All graphs depict mean ± SEM. *, *P* < 0.05 by two-tailed *t* test or one-way ANOVA as appropriate. ns, not significant.

identified in vehicle or RT samples (Fig. 6A and B; Supplementary Fig. S6C). We named these FAKi treatment–induced CAFs FAK.CAF.1, FAK.CAF.2, FAK.CAF.3, and RTFAK.CAF based on the treatments that induced them (Fig. 6B; Supplementary Fig. S6B). These FAKi-induced phenotypic clusters were also seen with multiple data normalization and integration strategies, suggesting these phenotypic population shifts were not due to batch or computational effects but rather a treatment-induced shift in transcriptional phenotype (Supplementary Fig. S6D–S6F). We observed that FAKi-induced CAF subsets became enriched in FAKi-treated samples at the expense of myCAF subsets (Fig. 6B;

Supplementary Fig. S6B and S6D–S6F). Additionally, we observed a decreased number of αSMA⁺ CAFs by IHC and collagen density by Sirius Red staining in both FAKi- and RT + FAKi-treated mice compared with controls (Fig. 6C and D). These data suggest that FAKi treatment significantly altered the CAF composition/phenotype.

To further elucidate the phenotypic differences in these CAF subsets, we performed GSEA and overrepresentation analyses comparing CAFs in vehicle-treated mice to CAFs in FAKi-treated mice. In comparison with CAFs from vehicle-treated mice, CAFs from FAKi-treated mice upregulated pathways associated with TNFα, IFNγ, inflammatory response, ROS, IL6 and IL2 signaling, and T-cell activation while downregulating pathways associated with epithelial-to-mesenchymal transition, angiogenesis, TGFβ, MTORC1 signaling, oxidative phosphorylation, and glycolysis (Fig. 6E and F; Supplementary Fig. S6G and S6H). As expected, we also saw downregulation of FAK and integrin signatures in CAFs in FAKi-treated mice (Fig. 6F; Supplementary Fig. S6H).

To confirm that we retained the same antitumor phenotypes generated by FAKi treatment, we performed GSEA and overrepresentation analyses comparing CAFs in vehicle-treated mice with CAFs from RT + FAKi-treated mice. In comparison with vehicle, RT + FAKi-treated mice upregulated pathways associated with TNFα, IFNγ, and inflammatory response, similar to CAFs from FAKi-treated mice. Furthermore, the addition of RT to FAKi resulted in the upregulation of pathways associated with IFNα (Fig. 6G–I). We also observed downregulation of TGFβ, MYC, integrins, MAPK, GMCSF, VEGFR, FAK signaling, and DNA-repair pathways as well as upregulation of leukocyte migration and chemotaxis (Fig. 6G-I; Supplementary Fig. S6I). To cross-validate the upregulation of IFN signaling in CAFs, we performed mIHC for CK19, PDPN, and pSTAT1 and found an upregulation of pSTAT1⁺ CK19⁻ PDPN⁺ CAFs in RT + FAKi-treated mice (Fig. 6J).

Several CAF subsets have been identified in human PDAC with potential immunomodulatory activity and unique origins. These include CD105⁺ (62), LRRC15⁺ (63), and NetrinG1⁺ CAFs (64), as well as pancreatic stellate cell (PSC)–derived CAFs (65). To understand how our treatments affected these subsets, we analyzed previously defined signatures for these CAF subsets using an averaged Z-score (Seurat's "AddModuleScore") or specific marker genes. Unfortunately, we could not detect sufficient levels of NetrinG1 or PSC-derived transcripts to reach a conclusion for these subsets. However, gene signature–positive or marker gene–positive CD105⁺ CAFs and LRRC15⁺ CAFs were decreased in both FAKi and RT + FAKi–treated PDAC tumors (Fig. 6K and L; Supplementary Fig. S6J and S6K). Taken together, these data suggest that inhibition of FAK signaling remodeled the PDAC CAF phenotype to augment IFN signaling in the stroma, which may facilitate antitumor immunity.

## FAK Inhibition in Combination with RT in PDAC Patients Activates IFN Signaling

Based on the data above, we initiated a clinical trial of a FAKi (defactinib; VS-6063) in combination with SBRT in patients with locally advanced PDAC (NCT04331041). In the patients from the phase I safety lead-in cohort, we performed scRNA-seq on tissues from pre- and posttreatment biopsies

(Fig. 7A). In data from the first five patients, UMAP analysis identified PDAC cells, CAFs, and major immune populations (Fig. 7B; Supplementary Fig. S7A). Mirroring what we found in our preclinical studies (Fig. 3), differential gene pathway analysis of the PDAC cells showed that the combination treatment led to upregulation of inflammatory response, IFN, TNFα signaling, T-cell activation, and phagocytosis pathways and downregulation of MYC pathways (Fig. 7C; Supplementary Fig. S7B). These data suggest that RT + FAKi might halt PDAC proliferation and augment immunogenicity. To further understand how SBRT + VS-6063 treatment changed the TME in our patients, we reclustered the CAFs, T cells, and TAMs separately and compared differentially expressed genes and pathways in these pre- and posttreatment biopsies. In CAFs, we observed that SBRT + VS-6063 increased the IFNα, IFNβ, TNFα signaling, and T-cell activation pathways, and decreased the TGFβ and integrin signaling pathways (Fig. 7D; Supplementary Fig. S7C–S7F). Similarly in T cells, we observed increases in IFNα, IFNβ, and TNFα pathways, and in TAMs we observed increases in IFNα, IFNβ, and ROS pathways, and decreases in glycolysis and MTORC1 pathways in SBRT + VS-6063 posttreatment samples (Fig. 7E-G; Supplementary Fig. S7G–S7I). These results from CAFs, T cells, and TAMs in humans parallel our results obtained in mice, which demonstrate activation of IFN signaling in both the target tumor compartment and the tumor-associated stroma.

## FAK Inhibition in Combination with RT Renders Checkpoint Blockade Effective

Our data suggest that adding FAK inhibition to RT led to tumor regression and priming of tumor antigen–specific T cells (Fig. 4B–D, G, I, and J; Supplementary Fig. S4A–S4D and S4G). However, these effects in turn drove the upregulation of T-cell exhaustion (Fig. 5N–R; Supplementary Fig. S5N). This suggests that these newly primed CD8⁺ T cells might become limited by checkpoints. To test this, we treated mice bearing established syngeneic KP2-OVA-GFP PDAC tumors with RT + FAKi in combination with αPD-1 and αCTLA4 IgGs [immune-checkpoint blockade (ICB); Fig. 7H]. Mirroring our T-cell depletion studies, short-term tumor regression by RT + FAKi was not affected by the addition of ICB (Fig. 7I); however, the triple combination of RT + FAKi + ICB led to progressive tumor regression over time and long-term survival in 8 of 9 mice in the treatment group, which was superior to all other treatment groups (Fig. 7J). We next compared the effector phenotype of T cells in these mice. We found that the addition of FAKi to RT + ICB resulted in higher numbers of IFNγ- and TNFα-expressing CD8⁺ and CD4⁺ T cells (Fig. 7K). Furthermore, the CD4⁺ T cells from these RT + FAKi + ICB-treated mice were skewed toward CD4⁺ T effector cells instead of CD4⁺ FOXP3⁺ T regulatory cells (Fig. 7K; Supplementary Fig. S7J). We repeated this in the KI PDAC model and observed that the addition of ICB to RT + FAKi also sustained more durable tumor regression (Supplementary Fig. S7K and S7L). Our mechanistic mouse models and human data suggest that combining FAK inhibition with RT can reprogram the TME to support IFN signaling and tumor immunity (Fig. 7L). These preclinical checkpoint combination data also suggest that the changes brought by RT + FAKi could be further enhanced with the addition of checkpoint immunotherapy.
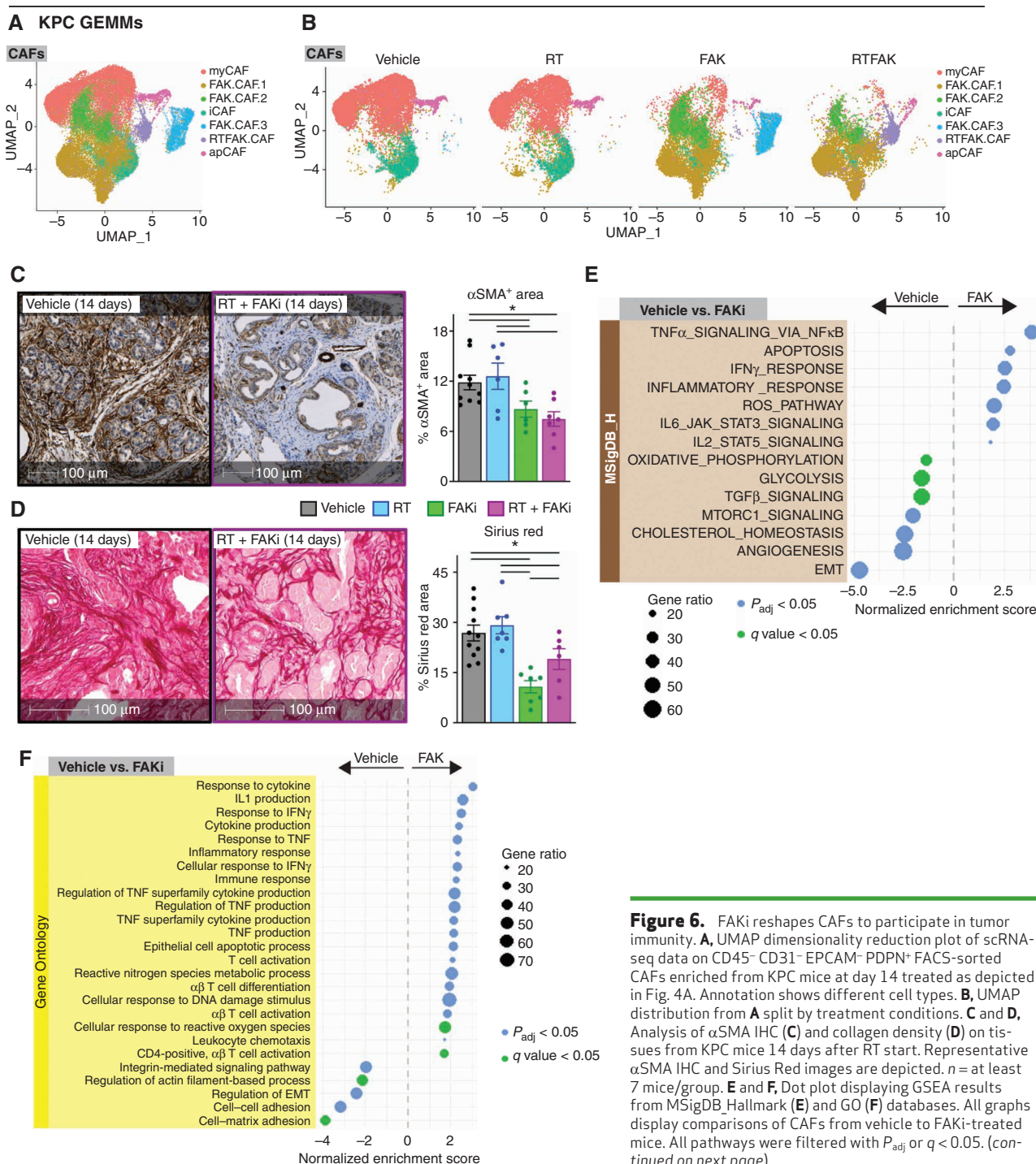
**Figure 6.** FAKi reshapes CAFs to participate in tumor immunity. **A,** UMAP dimensionality reduction plot of scRNA-seq data on CD45⁻ CD31⁻ EPCAM⁻ PDPN⁺ FACS-sorted CAFs enriched from KPC mice at day 14 treated as depicted in Fig. 4A. Annotation shows different cell types. **B,** UMAP distribution from **A** split by treatment conditions. **C** and **D,** Analysis of αSMA IHC (**C**) and collagen density (**D**) on tissues from KPC mice 14 days after RT start. Representative αSMA IHC and Sirius Red images are depicted. *n* = at least 7 mice/group. **E** and **F,** Dot plot displaying GSEA results from MSigDB_Hallmark (**E**) and GO (**F**) databases. All graphs display comparisons of CAFs from vehicle to FAKi-treated mice. All pathways were filtered with $P_{adj}$ or $q < 0.05$. (*continued on next page*)

## DISCUSSION

Many factors contribute to the recalcitrant nature of PDAC (2, 15–18). Here, we show that the PDAC stroma can drive RT resistance. Our findings are in agreement with several other studies, which highlight the critical role of β1 integrin (60, 66, 67) and Caveolin (68) signaling in regulating RT sensitivity in multiple cancer models. ECM can affect RT response by several mechanisms, including directly signaling to tumor cells through integrins and other receptors (58–60, 69, 70), acting as

a reservoir for secreted mitogens (71–73), and serving as a major regulator of oxygen bioavailability (74, 75). Although these studies showed that the stromal ECM can promote the survival of cancer cells following RT, it remains unclear how the PDAC stroma might affect RT-induced immune priming. Interestingly, our data suggest that collagen-rich ECM not only promotes cancer cell survival but also represses RT-induced IFN signaling that may be critical to RT-induced tumor immunity.

In our studies using KPC GEMMs, we found that although RT resulted in temporary short-term tumor control, it failed to
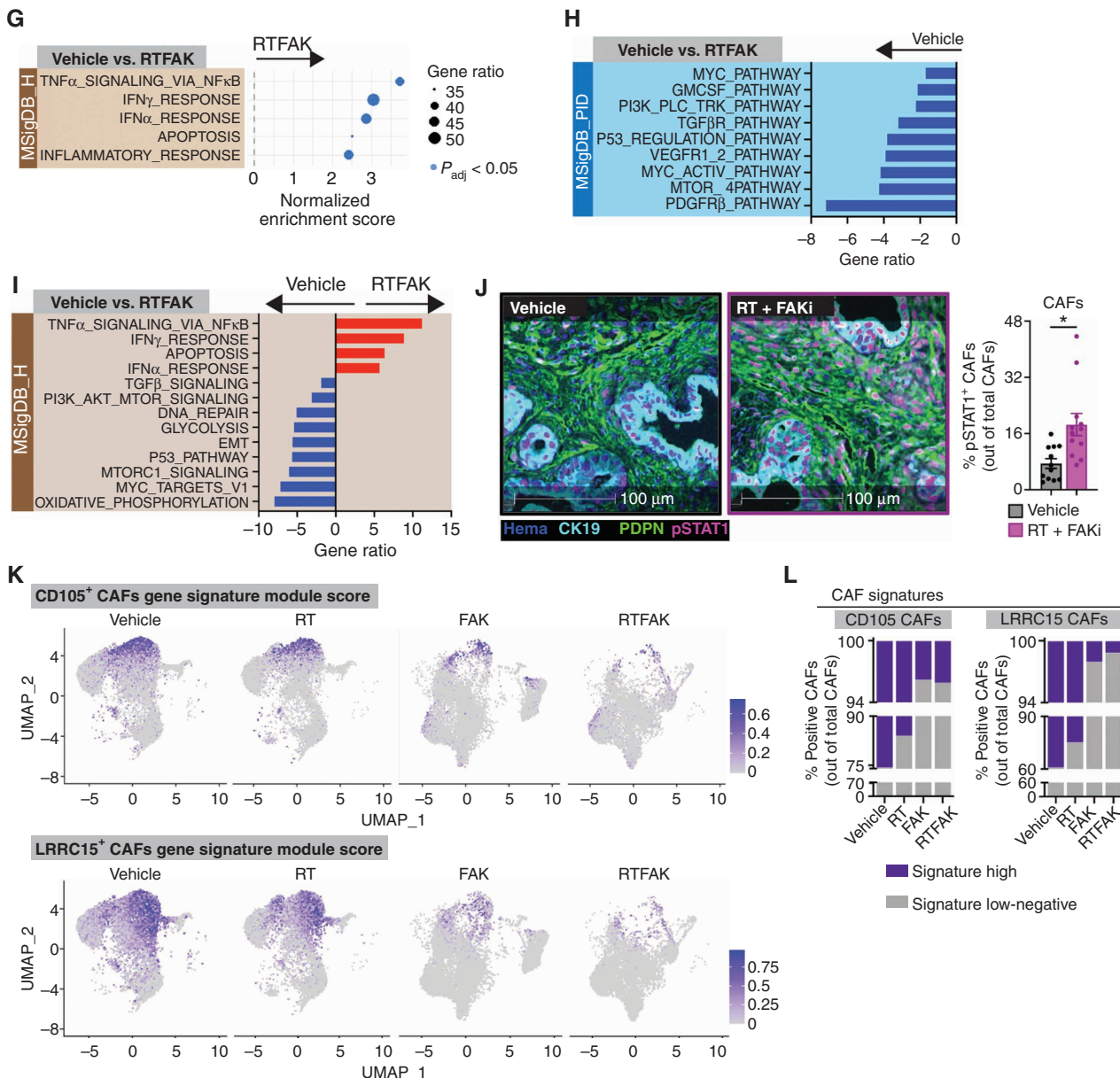
**Figure 6.** *(Continued)* **G–I,** Dot plot displaying GSEA results from MSigDB_Hallmark database (**G**) and bar graphs displaying overrepresentation analysis of DEGs on CAFs in **A** to known biological functions in MSigDB_PID (**H**) and MSigDB_Hallmark (**I**) databases. All graphs display comparisons of CAFs from vehicle mice to RT + FAKi-treated mice. All pathways were filtered with $P_{adj} < 0.05$. **J,** mIHC analysis of CK19⁻ PDPN⁺ pSTAT1⁺ cells in tissues of KPC mice from Fig. 4A. Representative CK19, PDPN, and pSTAT1 fused mIHC images are depicted. $n =$ at least 6 mice/group. **K,** UMAP representation of CD105⁺ CAF or LRRC15⁺ CAF gene signature module scores mapped onto CAFs in **A** and **B**. **L,** Quantification of CAFs in **A** for CD105⁺ CAF gene signature or LRRC15⁺ CAF gene signature. All graphs depict mean ± SEM. *, $P < 0.05$ by two-tailed *t* test or one-way ANOVA as appropriate.

prime T-cell responses. This was translated to a failure of long-term tumor control and no survival benefit. This is noteworthy because RT is highly capable of priming T cells and controlling tumor growth in other cancer models (76, 77), including the *Kras/Trp53*-driven sarcomas we presented here. Even though our PDAC and sarcoma GEMMs carry the same driver mutations in *Kras* and *Trp53*, we noted a major difference in the amount of stromal desmoplasia; the PDAC stroma is highly desmoplastic compared with genetically equivalent sarcomas. In our current study, we found collagen and pancreatic fibroblasts cooperatively mitigated RT efficacy and induction of

tumor cell death *in vitro*, which was in part mediated through fibroblasts' support of PDAC cell proliferation and collagen's ability to blunt RT-induced IFN signaling (Fig. 2). Similar interactions have been reported, in which PSCs' secreted factors, such as IL1α and TGFβ, enhance PDAC cell proliferation, migration, invasion, and colony formation, and drive resistance to gemcitabine and RT through MAPK and AKT signaling (78). Furthermore, PSCs can directly interact with PDAC cells to promote radioprotection and stimulate tumor cell proliferation through β1 integrin signaling, which is independent of phosphoinositide 3-kinase but depends on FAK
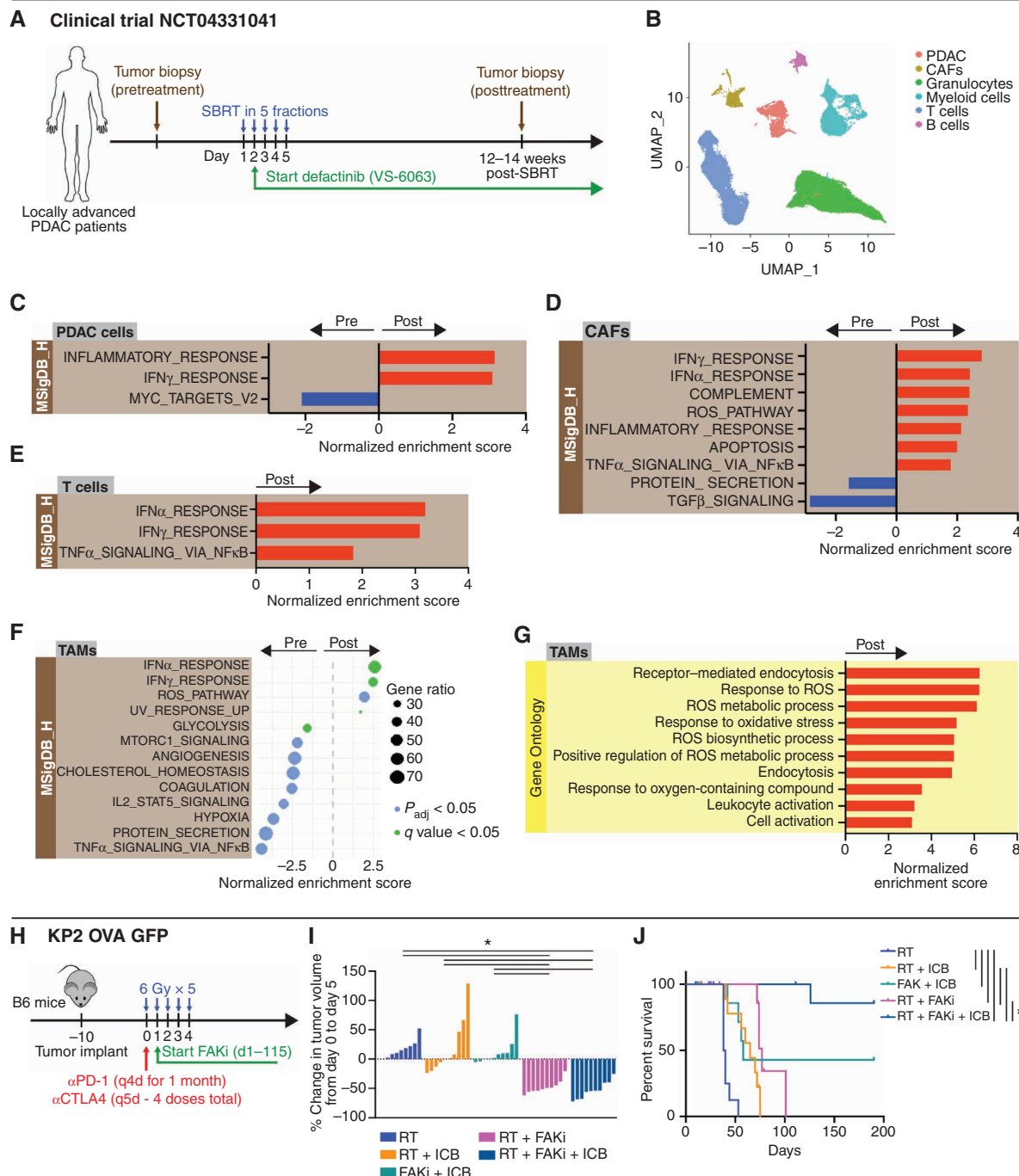
**Figure 7.** FAK inhibition in combination with RT in patients with PDAC activates IFN signaling. **A,** Schematic of the clinical trial (NCT04331041). Patients received SBRT with a total of 50 Gy given in 5 fractions. Defactinib (VS-6063) was given at a dose of 400 mg twice a day starting at the end of day 2 after SBRT and continued up to one year. Tissues were obtained pretreatment and 12 to 14 weeks after SBRT. **B,** UMAP analysis of eight pre- and posttreatment biopsies from **A**. **C,** Bar graph displaying GSEA of DEGs on all the PDAC cells in **B** to known biological functions in MSigDB_Hallmark database. All graphs display comparisons of pretreatment to posttreatment biopsies. All pathways were filtered with $P_{adj} < 0.05$. **D,** Bar graph displaying GSEA of DEGs on all the CAFs in **B** to known biological functions in MSigDB_Hallmark database. All graphs display comparisons of pretreatment to post-treatment biopsies. All pathways were filtered with $P_{adj} < 0.05$. **E,** Bar graph displaying GSEA of DEGs on all the T cells in **B** to known biological functions in the MSigDB_Hallmark database. All graphs display comparisons of pretreatment to posttreatment biopsies. All pathways were filtered with $P_{adj} < 0.05$. **F,** Dot plot displaying GSEA of DEGs on all the TAMs in **B** to known biological functions in MSigDB_Hallmark database. All graphs display comparisons of pretreatment to posttreatment biopsies. All pathways were filtered with $P_{adj} < 0.05$ or $q$ value $< 0.05$. **G,** Bar graph displaying GSEA of DEGs on all the TAMs in **B** to known biological functions in the GO database. All graphs display comparisons of pretreatment to posttreatment biopsies. All pathways were filtered with $P_{adj} < 0.05$. **H,** Schematic of RT (6 Gy × 5), FAKi (75 mg/kg twice a day), and ICB (αPD-1, 200 µg and αCTLA4, 200 µg) administration in KP2-OVA-GFP tumor–bearing mice. Mice were treated and longitudinally assessed for tumor burden. **I,** Waterfall plot of KP2-OVA-GFP tumor-bearing mice from **H** evaluating tumor growth difference from day 0 to 5. $n = 10$ mice/group. **J,** Kaplan–Meier survival curve of KP2-OVA-GFP mice from **H**. $n = 10$ mice/group. (*continued on next page*)
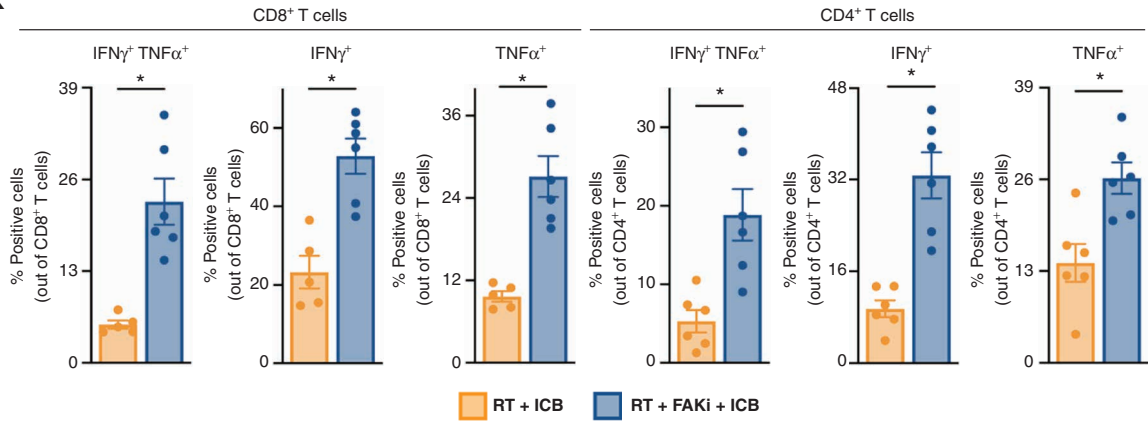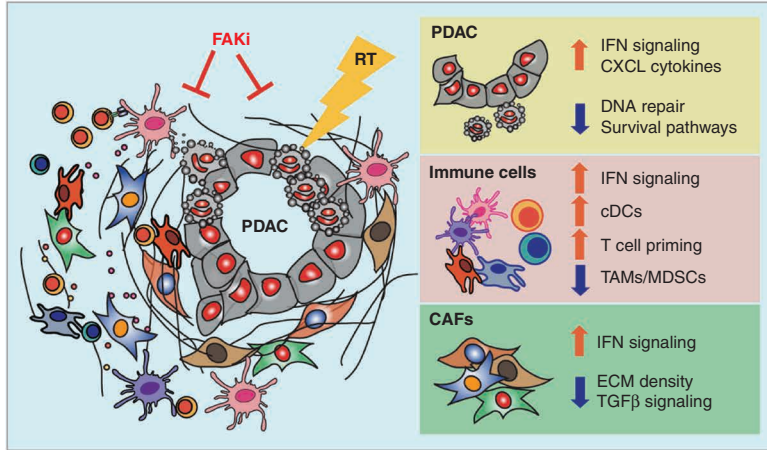
**Figure 7.** *(Continued)* **K,** Functional assay of CD8+ and CD4+ T cells by flow cytometry from mice treated as in **H**. Tumors were isolated on day 10 after the start of treatment. Bar graphs showed quantification of IFNγ ± TNFα-positive CD8+ and CD4+ T cells. $n$ = at least 6 mice/group. **L,** Graphical abstract of primary findings. For comparison between multiple groups; *, $P < 0.05$ by two-tailed $t$ test, one-way ANOVA, or Kaplan–Meier as appropriate.

(66, 79). The presence of extensive desmoplasia and its role in promoting tumor proliferation in PDAC further explains why, unlike in sarcoma, RT counterintuitively increases PDAC tumor cell proliferation after resistance occurs. This suggests that RT may perform differently in a tumor that is stroma-rich versus stroma-light, and these differences are partly mediated by ECM–receptor FAK signaling.

Retrospective studies of surgical resections have shown that higher levels of fibrosis post–neoadjuvant treatment are correlated with better pathologic response and improved survival (80, 81). Conversely, we found that collagen and fibroblasts in treatment-naïve tumors additively blunt RT efficacy, which suggests that treatment-naïve and posttreatment desmoplasia could have distinct characteristics and effects, the earlier of which can affect treatment response. It may be more relevant to assess posttreatment PDAC fibrosis/desmoplasia in the context of canonical FAK activation as an indicator of the downstream ECM–receptor signaling effects of collagen deposition.

Prior studies have demonstrated that inhibition of FAK signaling in PDAC changes the phenotype of both tumor cells and stromal cells (40, 46, 47, 82). This prompted us to see if FAKi could overcome stromal-induced protection to result in RT-induced tumor death. To our surprise, we found that FAKi reversed RT resistance in PDAC, and these effects corresponded with changes in DNA damage repair/responses, ROS pathways, cell-cycle regulation, and inflammatory signaling (Fig. 3). Similarly, in melanoma and lung cancer, FAKi can resensitize tumor

cells to RT by modulating DNA damage responses (83) and NFκB activity (40). These FAKi-specific pathways in tumor cells may play a role in promoting RT efficacy in PDAC. Our *in vitro* RNA-seq and proteomics studies focused on signaling in the cancer cells alone; however, the biological effects of FAKi and RT are not limited to the cancer cells. The role of these therapies in shaping PDAC stromal cells, particularly fibroblasts, is noteworthy and impactful. Indeed, scRNA-seq data from KPC GEMMs and human patients with PDAC suggest significant changes in stromal phenotype and potentially tumor–stromal interactions. Further work needs to be done to disentangle the cell type– and tissue-specific differences in FAK signaling and their respective contributions to RT resistance.

Aside from tumor cell–directed effects of the combination treatment, we likewise found that in the presence of FAKi, RT could induce immune priming. This was marked by the increase in tumor-infiltrating cDC1s and tumor antigen–specific T cells, along with shifts in TAMs, cDCs, and T-cell phenotypes toward being more antitumor. We also found an increase in both type I and II IFN responses/pathways in the dual RT + FAKi treatment, but not in either RT or FAKi monotherapy alone. We postulate that these changes in tumor immunity facilitate RT's ability to prime better antitumor T-cell responses, both in the targeted tumor tissue and systemically. One possible explanation for the ability of FAK inhibition to rescue RT-induced immune priming is through altering collagen interactions in the stroma and how they contribute to IFN signaling.

CAFs are another major contributor to the stromal modulation of RT treatment response in PDAC (14, 27–29). Similarly, CAFs have been implicated in PDAC resistance to both chemotherapies and immunotherapies (30–33). However, the distinct roles of CAF subpopulations in therapeutic resistance mechanisms have yet to be fully elucidated (84–86). For example, the extent to which CAF subtypes are interchangeable is unclear, and further study is needed to determine what dictates their numbers, distribution, and function during treatment. Interestingly, we found that RT + FAKi causes significant changes in the composition of CAFs, which raised the possibility that these CAFs may participate productively in antitumor immunity. Previous studies have shown that CAFs can play a role in tumor immunity through IL1, TGFβ, and IL6 signaling (14, 28, 29, 87), and our study identifies a novel role for CAFs in antitumor immunity through IFN signaling. We also found that CAFs in the RT + FAKi-treated mice downregulated TGFβ signaling, which has been shown to be a key signaling pathway in the protumor CD105$^+$ CAFs (62), αSMA$^+$ myCAFs, and LRRC15$^+$ CAFs (63). Accordingly, we found FAKi decreased both CD105 and LRRC15 gene signature–expressing CAFs, which suggests a potential shift toward antitumor phenotype. Although NetrinG1$^+$ and PSC-derived CAFs have both been identified (64, 65), our data on these subsets was inconclusive. It will be interesting to address the role and origin of CAF heterogeneity in FAKi efficacy as more relevant tools are established. Important for this may also be identifying the CAF-intrinsic versus cancer cell–driven roles of FAK signaling in shaping CAF heterogeneity.

Overall, this study suggests that stromal modulation by FAKi sensitizes PDAC to RT-induced antitumor immunity in both the immune and stromal compartments (Fig. 7L). Furthermore, in combination with FAKi, RT unlocks sustained checkpoint immunotherapy efficacy, which is translated into long-term tumor control and/or eradication. Based on our findings, we are currently testing the clinical efficacy of FAK inhibition in combination with SBRT in patients with locally advanced PDAC (NCT04331041), which to this point has mirrored many of the biomarker findings presented in mouse models. Perhaps most significantly, our data strongly support the addition of ICB, which may be critical for the prevention of metastatic disease in these patients with PDAC.

## METHODS

### Genetic Mice and Other Models

KPC and KPC-OG mice used in these studies were bred to C57BL/6J background and verified by congenic markers. The generation and studies entailing the details of the KPC-OG mouse were published by our lab (54). KPC and KPC-OG mice were enrolled for treatment studies when the first >0.5 cm tumor was detected by biweekly palpation corroborated by ultrasound measurement. Thereafter, tumor size was assessed weekly by ultrasound (SonoSite m-Turbo). Survival events were scored when mice lost >15% body weight, tumor burden reached >1.8 cm in diameter, moribund appearance, severe cachexia, or per absolute survival. For all studies, care was taken to include negative littermates as well as sex- and age-matched in the same experimental setup.

*LSL-Kras*$^{G12D}$/*Trp53*$^{Flox/Flox}$/*OVA-GFP*$^+$ mice, littermates of KPC-OG mice, were injected with Adenoviral-Cre at 8 to 10 weeks old, which generated sarcoma GEMMs (KPS-OG) 7 to 8 weeks

after inoculation. Tumor size was assessed by caliper measurement for randomization.

All animal studies were approved by the Washington University Institutional Animal Care and Use Committee review board.

### Human Subjects

All human PDAC tissues were obtained under written informed consent from the patients. The Washington University Ethics Committee approved the study in accordance with recognized ethical guidelines, and studies were conducted under institutional review board protocol #201108117 and #201704078 and clinical trial NTC04331041.

### Cell Lines

Three-dimensional organoid cell lines (KPOG) were derived from tumor-bearing female KPC-OG mice. KRAS-INK or KI cells used in certain orthotopic transplant experiments were derived from *Pdx1-Cre/ LSL-Kras*$^{G12D}$/*Ink/Arf*$^{Flox/Flox}$ mice in Dr. Hanahan's laboratory (EPFL, Lausanne). KP2 cells were derived from PDAC tumor tissue obtained from 6-month-old *p48-Cre/LSL-Kras*$^{G12D}$/*Trp53*$^{Flox/+}$ mice, which were screened for C57BL/6 identity. Cells were grown out on collagen-coated plastic for <12 passages and were tested for CK19, αSMA, Vimentin, and CD45 to verify their identity and purity. KP2-OVA-GFP cells were derived from tumor-bearing female KPC-OG, which were used in certain syngeneic subcutaneous experiments. PDA.69 cells were derived from *Pdx1-Cre/LSL-Kras*$^{G12D}$/*Trp53*$^{R172H/+}$ mice as previously published (50). A single lot of frozen cells was used for all experiments. These cells were banked and last tested for *Mycoplasma* using two independent commercial kits (Sigma and Lonza) in June 2019.

Three independent wild-type (WT) pancreatic fibroblast primary cell lines were derived from WT C57BL/6J background mice. Pancreata were harvested (detailed below) and plated on tissue culture flasks under standard antibiotics and the addition of Gentamycin and Amphotericin B. No additional growth factors were supplemented in culture media. After ~3 passages, the culture was composed of pure fibroblasts only. For organoid growth studies, only fibroblasts with passage <10 were used. Fibroblast purity was tested by flow cytometry for PDPN as a pan-marker of fibroblasts. All cell lines were tested negative for *Mycoplasma*.

Two independent CAF lines were derived from end-staged KPC-OG mice. Following tissue digestion, single-cell suspension was resuspended in flow cytometry buffer and stained with fluorophore-conjugated antibodies as detailed below. Cells were sorted for CAFs (GFP$^-$ CD45$^-$ CD31$^-$ EPCAM$^-$ PDPN$^+$) using FACSAria-II (BD Biosciences), and replated in a complete medium until stable cell lines were established. CAF purity was tested by flow cytometry for EPCAM$^-$ and PDPN$^+$ as a pan-marker of fibroblasts. All cell lines were tested negative for *Mycoplasma*.

Tumor cell suspension derived after tumor harvest (detailed below) was plated on collagen-coated tissue culture flasks under standard antibiotics for the generation of 2D cell culture. Cell suspension derived after tumor harvest (detailed below) was plated on Matrigel (Cultrex Organoid Qualified BME, Type 2) dome under standard antibiotics for the generation of 3D organoid cell culture. Protocol for the generation of 3D organoid cell culture was adapted from Dr. Tuveson's laboratory (Cold Spring Harbor Laboratory; ref. 88). GFP$^+$ tumor cells were sorted on FACSAria-II (BD Biosciences), and replated in complete medium until stable cell lines were established. All 2D cell lines were cultured in complete medium [DMEM-F12 with 10% fetal bovine serum (FBS) and 1% penicillin and streptomycin] at 37°C and 5% $CO_2$. All 3D cell lines were cultured in complete medium (Advanced DMEM-F12 with 1% HEPES, 1% L-glutamine, and 1% penicillin and streptomycin) at 37°C and 5% $CO_2$. All cell lines were passaged <6 times and were tested positive for cytokeratin-19, and negative for smooth muscle actin and vimentin to verify their carcinoma identity and purity. All cell lines were tested negative for *Mycoplasma*.

### Tissue Harvest

Mice were euthanized by trans-cardiac perfusion using 15 mL of PBS-heparin under isoflurane anesthesia. When taken for histology, tumor tissues were fixed in 10% neutral-buffered formalin overnight at 4°C. When taken for cellular assays, tumor tissues or respective lymph nodes were manually minced and digested in 20 mL of sterile 1× Hank's Balanced Salt Solution (HBSS; Thermo Fisher) containing 2 mg/mL of collagenase A (Roche) and 1× DNase I (Sigma) for 30 minutes at 37°C with constant stirring. Digestion was quenched in 5 mL of sterile FBS (Atlanta Biologicals) filtered through 40-µm Nylon mesh, pelleted through centrifugation (2,000 RPM for 5 minutes at 4°C), and resuspended in required media/buffer as single-cell suspensions.

### Orthotopic and Syngeneic Implantations

Age-matched 6- to 8-week-old female C57BL/6 and FVB/NJ mice were used for orthotopic/transplantable mouse models. Syngeneic orthotopic PDAC tumors were established by surgical implantation, as previously described (46). To establish orthotopic models, 100,000 KI or KP2 cells in 50 µL of Cultrex (Trevigen) were injected into the pancreas of sex-matched C57BL/6 or FVB/NJ mice as previously described (89). Cohorts of mice were randomized into different treatment groups by gross tumor diameter using thrice-weekly palpation, external caliper measurement, and ultrasound measurement. To establish subcutaneous models, 250,000 KP2 or KP2-OVA-GFP cells or 100,000 PDA.69 cells in 50 µL of Cultrex (Trevigen) were injected into the mammary fat pad of sex-matched C57BL/6 mice as previously described. Cohorts of mice were randomized into different treatment groups by gross tumor diameter using thrice-weekly external caliper measurement.

### Pharmacologic Inhibitors

FAKi (VS-4718), provided by Verastem, Inc., is a selective bispecific inhibitor with activity against FAK1/PTK2 and PYK2/PTK2β kinases. Cell-based assays have determined it has biochemical half-maximal inhibitory concentrations ($IC_{50}$) of 6.0 and 20 nmol/L for FAK and PYK2. For animal experiments, 75 mg/kg VS-4718 was formulated in vehicle [0.5% carboxymethyl cellulose and 0.1% Tween-80 (Sigma-Aldrich) in sterile water] and administered by oral gavage twice a day. For in vitro studies 0.25, 0.5, or 1.0 µmol/L of VS-4718 in DMSO was used.

### Radiotherapy

Mice received RT as five daily hypofractionated doses (6 Gy × 5) using the Small Animal Radiation Research Platform (SARRP200, XStrahl Life Sciences). Mice were injected intraperitoneally (i.p.) with an iodine contrast agent (2,100 mg/kg) before being placed on the irradiation platform one at a time under isoflurane anesthesia. Conebeam CT imaging was performed for each individual mouse to pinpoint the pancreas, images were imported into Muriplan and used to select an isocenter. The tumor was then irradiated using anterior–posterior-opposed beams using either the 5 mm × 5 mm or 10 mm × 10 mm collimator at a dose rate of 3.9 Gy/minute. Mice were monitored over 2 weeks for signs of radiation sickness or weight loss. DietGel Recovery gel was provided for a 14-day window immediately following radiotherapy in survival studies.

For in vitro radiation experiments, RS2000 160 kV X-ray Irradiator using a 0.3-mm copper filter (Rad Source Technologies) was used.

### Immunotherapeutic Neutralizing Antibodies

For the immunotherapy regimen, 250 µg of agonist antibodies (αCTLA4 clone UC10-4F10-11; αPD-1 clone RMP1-14; Bio X Cell) was given by i.p. injection; αPD-1 was given every 4 days for a total of 30 days and αCTLA4 was given every 5 days for a total of 4 doses from the beginning of treatment. Treatments were discontinued after 30 days to prevent α-rat IgG reaction.

For T-cell depletion, CD4 or CD8 neutralizing IgG antibodies (αCD4 clone GK1.5; αCD8 clone 2.43, Bio X Cell) were administered, with first injection (at day −2) containing 400 µg and subsequent injections (every 4 days) containing 200 µg of each IgG. Treatments were discontinued after 30 days. As control, rat IgG2β isotype control (clone LTF-2, Bio X Cell) was administered.

For type I IFN neutralization, αIFNAR1 (clone MAR1-5A3, Bio X Cell) antibody was administered, with first injection (at day −2) containing 750 µg and subsequent injections (every 3 days) containing 250 µg of each IgG. Treatments were discontinued after 30 days. As control, mouse IgG1 isotype control (clone MOPC-21, Bio X Cell) was administered.

### Organoid Cultures

Three-dimensional organoid cell lines derived from KPC-OG mice, called KPOG, were passaged in Cultrex Organoid Qualified BME, Type 2. Pancreatic fibroblasts were derived from C57BL/6J mice. Organoid cells (~50 structures in a dome of 50 µL of Cultrex Organoid Qualified BME, Type 2) were cultured with or without 100,000 pancreatic fibroblasts or FACS-sorted CAFs per dome. Collagen I concentrations (1.0 mg/mL) were modulated in the ECM. One day after organoid culture preparation, organoid cultures were treated with FAKi at varying dose concentrations. Two hours after FAKi treatment, the culture was treated with radiation.

All organoid experiments were done in 24-well tissue culture–treated plates. At least $n = 3$/group was used for statistical power analysis. KPOG organoid growth was monitored using the GFP marker. Fluorescence images were taken using a Nikon AZ100 microscope daily, and images were analyzed using Metamorph and HALO imaging software for analyses.

### IHC Staining

Tissues were fixed in 10% neutral formalin for 18 to 24 hours, embedded in paraffin after graded-ethanol dehydration, and sectioned into 5-µm sections using a microtome. Where applicable, formalin-fixed, paraffin-embedded (FFPE) tissue sections were stained for hematoxylin and eosin (Thermo Fisher), Picro-Sirius Red (Sigma-Aldrich), and Masson's Trichrome (Diagnostic Biosystems) according to the manufacturer's instructions. Automated staining of tissues was carried out on the Bond RX^m (Leica Biosystems) following dewaxing and appropriate antigen retrieval. Immunostaining was chromogenically visualized using the Bond Polymer Refine Detection alone or in conjunction with Bond Intense R Detection Systems (DS9263, Leica Biosystems). Slides were dehydrated through graded ethanol, followed by xylene, then mounted using Xylene-based Cytoseal (Thermo Fisher) or Vectamount (Vector Labs) as appropriate.

Staining was performed with the following antibodies: αSMA (Abcam, ab5694), Podoplanin (BioLegend, 127402), Ki-67 (Abcam, ab15580), BrdUrd (Abcam, ab2284), CC3 (Cell Signaling Technology, 9661S), Cytokeratin 19 (DSHB TROMA-III), Cytokeratin 17/19 (Cell Signaling Technology, 12434S), CD8α (Cell Signaling Technology, 98941), pSTAT1 (Cell Signaling Technology, 8826s), CD4 (Abcam, ab183685), FOXP3 (eBioscience, 14-5773-82), and γH2Ax (Cell Signaling Technology, 9718S).

### Flow Cytometry

Following tissue digestion, single-cell suspensions were resuspended in flow cytometry buffer (PBS containing 1% BSA and 5 mmol/L EDTA), FcR blocked with rat α-mouse CD16/CD32 antibodies (eBioscience) for 10 minutes and pelleted by centrifugation. Where applicable, CD8+ T cells specific for antigen OVA were labeled by incubating cell suspension with H2Kb::SIINFEKL-specific MHC I dextramer (1:5; Immudex protocol) for 10 minutes at room temperature prior to extracellular staining. Cells were consequently labeled with 100 µL of fluorophore-conjugated α-mouse extracellular antibodies at recommended dilutions for 25 minutes on ice. Intracellular staining for intracellular markers was conducted subsequently using the eBioscience Transcription Factor Staining buffer set, according to the

manufacturer's instructions. All antibodies are listed below. FCS data were acquired on BD Fortessa X-20 (BD Biosciences) within 3 to 4 days and analyzed using FlowJo software (v10).

For T-cell functional (cytokine release) assay, following tissue digestion, primary tumor cell suspension containing 100,000 cells was incubated in a 96-well plate with 1 μmol/L Brefeldin A (BioLegend) and 2 μmol/L Monensin Solution (BioLegend) and 1X Stimulation Cocktail (eBioscience) for 5 hours at 37°C and 5% $CO_2$. After incubation, cells were then labeled with fluorophore-conjugated anti-mouse antibodies as above.

Staining was performed with the following antibodies: CD45 (eBioscience, 25-0451), CD45 (BD Biosciences, 564225), CD3ε (eBioscience, 17-0031-82), CD11b (eBioscience, 56-0112-82), MHC-II (eBioscience, 48-5321-82), Ly6G (BioLegend, 127608), Ly6C (eBioscience, 45-5932), F4/80 (eBioscience, 15-4801-82), CD11c (eBioscience, 47-0114-82), CD24 (eBioscience, 11-0241-82), CD24 (eBioscience, 11-0242-82), CD103 (BioLegend, 121423), CD8α (BD Biosciences, 563786), CD8α (BD Biosciences, 562283), CD4 (eBioscience, 11-0043-82), CD62L (BioLegend, 104437), CD44 (eBioscience, 48-0441-82), PD-1 (eBioscience, 12-9985-82), TIM3 (BioLegend, 119715), Ki-67 (eBioscience, 50-5698-82), FOXP3 (eBioscience, 35-5773-82), MHC I (eBioscience, 11-5998-82), B220 (BioLegend, 103212), SIINFEKL Dextramer (Immudex, JD2163), IFNγ (BioLegend; clone XMG1.2), and TNFα (Invitrogen; clone MP6-XT22).

## Mass Cytometry

Tumors from KP2-OVA-GFP tumor-bearing mice were taken on day 14 after treatment start. Two to three tumors were pooled as one sample. Tumor samples were digested in HBSS supplemented with 2 mg/mL collagenase A (Roche), 2.5 U/mL hyaluronidase and DNase I at 37°C for 30 minutes with agitation to generate single-cell suspensions. Cell suspensions were counted and stained in 5 μmol/L cisplatin per million cells for exactly 3 minutes on ice and washed with Cy-FACS buffer (PBS, 0.1% BSA, 0.02% $NaN_3$, 2 mmol/L EDTA) twice. Cells were incubated with FcR blocking reagent plus surface-antibody cocktail for 40 minutes on ice. After incubation, surface-marker–stained cells were washed twice with Cy-FACS buffer. Cells were then fixed with 4% PFA for 10 minutes on ice and permeabilized for 40 minutes with permeabilization buffer (Invitrogen) containing the intracellular stain cocktail. All antibodies are listed below. Cells were then washed twice with PBS and stained with 200 μL of DNA intercalator per million cells. Cells were acquired on a CyTOF2 mass cytometer (Fluidigm), and data were uploaded to Cytobank for further analysis. Events were gated on singlets, live, and CD45$^+$. A maximum of 100,000 events were then visualized using the standard t-SNE algorithm. Populations of interest were manually gated and verified based on lineage marker expression.

Staining was performed with the following antibodies: CD45 (Fluidigm, 3089005B), CD90 (BioLegend, 105202), CD11c (Fluidigm, 3142003B), CD68 (BioLegend, 137001), MHC I (Fluidigm, 3144016B), CD206 (BioLegend, 141702), F4/80 (Fluidigm, 3146008B), MHC II (BioLegend, 107602), CD11b (Fluidigm, 3148003B), CD172α/SIRPα (BioLegend, 144002), Ly6C (Fluidigm, 3150010B), Ly6G (Fluidigm, 3151010B), CD64 (BioLegend, 139301), XCR1 (BioLegend, 148202), CD103 (BioLegend, 121402), NK1.1 (Bio X Cell, BE0036), BST2 (Novus/imgenx, DDX0390P-100), IRF4 (BioLegend, 646402), CD83 (Thermo Fisher Scientific, 14-0831-82), CD40 (Fluidigm, 124601), OX40L (BioLegend, 108802), CCR2 (R&D Systems, MAB55381-100), Cx3CR1 (Fluidigm, 3164023B), CCR7 (BioLegend, 120101), PD-L2 (Bio X Cell, BE0112), VISTA (BioLegend, 150202), Tim3 (Bio X Cell, BE0115), PDL1 (Bio X Cell, BE0101), CD80 (BioLegend, 104702), CD135/FLT3 (Thermo Fisher Scientific, 14-1351-82), CD86 (Fluidigm, 3172016B), TIM4 (BioLegend, 130002), B220 (Fluidigm, 3144011B), CD44 (Leinco, C382), GITR (Bio X Cell, BE0063), CD25 (Leinco, C1194), CD38 (eBioscience, 14-0381-82), CD90 (BioLegend, 105202), LAG3 (Leinco, L306), CD27 (eBioscience, 50-124-94), KLRG1 (Bio X

Cell, BE0201), CD103 (BioLegend, 121402), CD4 (Bio X Cell, BE0003-1), CD45 (Fluidigm, 3089005B), CD62L (Leinco, C2118), ICOS (eBioscience, 14-9949-82), OX40 (Bio X Cell, BE0031), PD-1 (eBioscience, 14-9981-82), TIGIT (Bio X Cell, BE0274), CD69 (eBioscience, 14-0691-82), TCRβ (Bio X Cell, BE0102), CD127 (Bio X Cell, BE0065), CD39 (BioLegend, 143802), NK1.1 (Bio X Cell, BE0036), CD8α (Leinco, C375), TCRγδ (eBioscience, 14-5711-82), TIM3 (Bio X Cell, BE0115), H2-Kb OVA (WUSTL CHiiPs core), Ki-67 (Novus, NBP2-22112), FOXP3 (eBioscience, 14-5773-82), GATA3 (eBioscience, 14-9966-82), Granzyme B (eBioscience, MA1-80734), CTLA4 (eBioscience, 50-129-16), TCF1 (R&D, MAB8224), ROR-γt (eBioscience, 14-6988-82), EOMES (eBioscience, 50-245-556), and T-bet (BioLegend, 644802).

## Western Immunoblot

Cell lysates were harvested using radioimmunoprecipitation assay (RIPA) lysis buffer (25 mmol/L Tris-HCl pH 7.5, 150 mmol/L NaCl, 1% NP-40, 0.5% DOC, 0.1% SDS) supplemented with protease and phosphatase inhibitors (Roche). Cell lysates were resolved in Tris-glycine sodium dodecyl sulfate/polyacrylamide gel electrophoresis (SDS/PAGE) gels and transferred to polyvinylidene difluoride (PVDF) membranes (Invitrogen). After blocking in 1X TBST buffer with 5% w/v BSA, membranes were probed with primary antibodies overnight at 4°C. Membranes were washed thrice in 1× TBST and probed with HRP-conjugated secondary antibody for 1 hour at room temperature. Membranes were developed with Pierce ECL Western Blotting Substrates and detected using a ChemiDoc XRS+ system (Bio-Rad).

Staining was performed with the following antibodies: β-actin (Cell Signaling Technology, 4970), pIRF3 (Cell Signaling Technology, 29047S), IRF3 (Cell Signaling Technology, 4302S), STING (Cell Signaling Technology, 13647S), and γH2Ax (Cell Signaling Technology, 9718S).

## RNA and cDNA Isolation

Total RNA was extracted from live cultured cells using an E.Z.N.A. Total RNA kit (OMEGA) according to the manufacturer's instructions and banked in −80°C until use. cDNA for downstream applications were synthesized using qScript cDNA SuperMix kit (QuantaBio) according to the manufacturer's instructions.

## RNA-seq and Analysis

RNA samples from treated KPOG organoid cultures were prepared according to the kit manufacturer's protocol, ribo-depleted using RiboZero protocol, and subsequently indexed, pooled, and sequenced on HiSeq 3000 (Illumina) at the Genome Technology Access Center, Washington University. Differential expression analysis of normalized counts (after standard base calling and demultiplexing) was performed to analyze for differences between conditions and the results were filtered for only those genes with Benjamini–Hochberg FDR adjusted $P \leq 0.05$. For each contrast extracted with *Limma*, global perturbations in known Gene Ontology (GO) terms and KEGG pathways were detected using the R/Bioconductor package *GAGE* to test for changes in expression of the reported log$_2$ fold changes reported for each term versus the background log$_2$ fold changes of all genes found outside the respective term.

## Mouse Tissue scRNA-seq Data Analysis

PDAC tissues were taken from vehicle-treated, RT-treated, FAKi-treated, or RT + FAKi-treated KPC pancreatic tumors 14 days after treatment start. Cells were sorted into two samples: Immune cells (CD45$^+$) and CAFs (CD45$^-$ CD31$^-$ EPCAM$^-$ PDPN$^+$) using Aria-II cell sorter (BD Biosciences). Each sample was generated from a pooled of 2–3 mice/treatment group. For a total of 4 treatment groups and 2 different cell types, we made 8 total libraries to be sequenced.

Sorted cells from each sample were encapsulated into droplets and libraries were prepared using Chromium Single Cell 3′v3 Reagent kits according to the manufacturer's protocol (10X Genomics). The generated libraries were sequenced by a NovaSeq 6000 sequencing system

(Illumina) to an average of 50,000 mean reads per cell. Cell Ranger mkfastq pipeline (10X Genomics) was used to demultiplex Illumina base call files to FASTQ files. Files from the KPC tumors were demultiplexed with >97% valid barcodes, and >94% q30 reads. Afterward, fastq files from each sample were processed with Cell Ranger counts and aligned to the mm10 reference (v.3.1.0, 10X Genomics, mouse reference mm10–2020-A from https://cf.10xgenomics.com/supp/cell-exp/refdata-gex-mm10-2020-A.tar.gz) to generate feature barcode matrix.

The filtered feature barcode matrices were loaded into Seurat (v4.1.2). For each Seurat object, genes that were expressed in less than 3 cells and cells that expressed less than 1,000 or more than 6,000 genes were excluded. Cells with greater than 10% mitochondrial RNA content were also excluded. SCTransform with default parameters was used on each individual sample to normalize and scale the expression matrix against the sequence depths and percentages of mitochondrial genes (90). Cell-cycle scores and the corresponding cell-cycle phase for each cell were calculated and assigned after SCTransform based on the expression signatures for S and $G_2$–M genes (CellCycleScoring). The differences between the S phase score and $G_2$–M score were regressed out by SCTransform on individual samples. Variable features were calculated for each sample independently and ranked, based on the number of samples they were independently identified (SelectIntegrationFeatures). The top 3,000 shared variable features were used for multiset canonical correlation analysis to reduce dimensions and identify projection vectors that defined shared biological states among samples and maximized overall correlations across datasets. Principal component analysis (PCA) was performed on the 3,000 variable genes calculated earlier (function RunPCA). Multiple datasets were then integrated using Harmony Integration (RunHarmony; ref. 91) using the calculated PCA values. Mouse immune cell datasets were integrated using Harmony (Fig. 5), mouse CAF datasets (Fig. 6) were not integrated, and mouse CAF Harmony integrated datasets are shown in Supplementary Fig. S6. A UMAP dimensional reduction was performed using the Harmony-corrected values to obtain a two-dimensional representation. Then, these defined 30 dimensionalities were used to refine the edge weights between any two cells based on Jaccard similarity (FindNeighbors) and were used to cluster cells through FindClusters functions, which implemented shared nearest neighbor modularity optimization. To characterize clusters, the FindAllMarkers function with $\log_2$ fold threshold = 0.25 and minimum 0.25-fold difference and MAST test was used to identify signatures alone with each cluster. Then the TAMs, cDCs, and adaptive immune cells (B cells, T cells, NK cells, $\gamma\delta$T cells) were selected and the top 3,000 variable features were recalculated to recluster using the above-described methodology. DEGs between the two groups were calculated for each dataset with min.pct of 0.1 and logfc.threshold of -Inf and MAST test (PrepSCTFindMarkers then FindMarkers). Then the DEG lists from each dataset were filtered with $P < 0.05$ and ranked based on fold change. These ranked gene sets were fed into GSEA to test for GO terms, KEGG pathways, Reactome and Molecular Signatures Database (MSigDB) gene sets with FDR <0.05 in ClusterProfiler (92).

### Human Sample scRNA-seq Data Analysis

PDAC tissues were taken from patients using ultrasound-guided biopsies, and details of the trial design are available on ClinicalTrials.gov (NCT04331041) and briefly here. Patients received SBRT with a total of 50 Gy given in 5 fractions. FAKi (VS-6063) was given at a dose of 400 mg twice a day starting at the end of day 2 after SBRT and continued up to one year. Tissues were obtained pretreatment and 12 to 14 weeks after SBRT. Biopsy tissues were processed and digested as described above. Following tissue digestion, processed cells from each sample were encapsulated into droplets and libraries using BD Rhapsody Single-Cell Capture and cDNA Synthesis Analysis System (BD Biosciences) according to the manufacturer's protocol. For a total of 6 pre- and posttreatment groups, we made 10 total libraries to be sequenced.

The generated libraries were sequenced by a NovaSeq 6000 sequencing system (Illumina) to an average of 50,000 mean reads per cell. FASTQ files from each sample were processed and aligned with BD Rhapsody WTA Analysis Pipeline (SevenBridges) using reference genome (GRCh38-PhiX-gencodev29.tar.gz) to generate a feature barcode matrix.

The filtered feature barcode matrices were loaded into Seurat as Seurat objects (Seurat v4). For each Seurat object, genes that were expressed in less than 3 cells and cells that expressed less than 1,000 or more than 6,000 genes were excluded. Cells with greater than 25% mitochondrial RNA content were also excluded. Seurat NormalizeData and ScaleData with default parameters were used on each individual sample to normalize and scale the expression matrix against sequence depth and percentage of mitochondrial genes. Variable features were calculated for each sample independently and ranked based on the number of samples they were independently identified (FindVariableFeatures). The top 3,000 shared variable features were used for multiset canonical correlation analysis to reduce dimension and identify projection vectors that define shared biological states among samples and maximize overall correlation across datasets. PCA was performed on the 3,000 variable genes calculated earlier (function RunPCA). Multiple datasets were then integrated using Harmony Integration (RunHarmony). A UMAP dimensional reduction was performed on the scaled matrix using the first 30 PCA components to obtain a two-dimensional representation of cell states. Then, these defined 30 dimensionalities were used to refine the edge weights between any two cells based on Jaccard similarity (FindNeighbors) and were used to cluster cells through FindClusters functions, which implemented shared nearest neighbor modularity optimization. To characterize clusters, the FindAllMarkers function with log fold threshold = 0.25 and minimum 0.25-fold difference and MAST test was used to identify signatures alone with each cluster. DEGs between the two groups were calculated for each dataset with min.pct of 0.1 and logfc.threshold of 0.01 and MAST test (FindMarkers). Then, the DEG lists from each dataset were filtered with $P < 0.05$ and ranked based on fold change. These ranked gene sets were fed into GSEA to test for GO terms, KEGG pathways, Reactome and Molecular Signatures Database (MSigDB) gene sets with FDR <0.05 in ClusterProfiler.

### RPPA

Cell extracts were lysed using (RIPA) lysis buffer (25 mmol/L Tris-HCl pH 7.5, 150 mmol/L NaCl, 1% NP-40, 0.5% DOC, 0.1% SDS) supplemented with protease and phosphatase inhibitors (Roche). Samples were then submitted to the MD Anderson Cancer Center for the RPPA assay. The Functional Proteomics RPPA Core is supported by MD Anderson Cancer Center Support grant # 5 P30 CA016672-40.

### Image Analysis

Whole-tissue scans at 10× or 20× magnification were obtained on a Zeiss Axio Scan Z1 brightfield/fluorescence Slide Scanner. Whole-tissue scans were analyzed with HALO software (Indica Labs) using area quantification, Cytonuclear, or HighPlex modules. Where noted, grading was conducted by a trained pathologist in a blinded fashion and verified by the principal investigator *post hoc*.

### mIHC

Serial staining was performed with multiple markers as indicated, adapted from a previously published study (93). FFPE tissue sections were loaded onto the BOND RX$^m$ autostainer (Leica Biosystems) for iterative staining cycles for markers, including CK19, CD8, CD4, FOXP3, PDPN, and pSTAT1. Slides were baked for 60 minutes and deparaffinized prior to the first cycle. Based on antibody host species, default manufacturer protocols and reagents were used up to labeling with HRP. Antigen labeling was chromogenically visualized with a ready-to-use AEC substrate (Abcam). Post-staining, the slides were

manually counterstained for hematoxylin, coverslipped using Vecta-Mount AQ Aqueous mounting media (Vector), then scanned using an Axio Scan Z1 (Zeiss). The slides were then decoverslipped and destained using an ethanol gradient, including a 1% hydrochloric acid wash, and blocked, as needed, with avidin/biotin blocking kit (Vector Laboratories) and anti-rabbit or anti-rat Fab fragments to eliminate carryover signal from previous cycles, prior to starting another staining cycle. Citrate-based antigen retrieval was performed before each staining cycle.

Images of the same specimen but different stains were cropped into multiple segments using ZEN software (Zeiss). Using HALO image analysis software (Indica Labs), each marker was then converted into pseudocolors using the Deconvolution algorithm and compiled into composite multimarker images. Markers of interest were pseudo-colored and quantified through the HighPlex FL algorithm in HALO software.

### Statistical Analysis

All statistical analyses were performed using GraphPad Prism software v9, with input from a Biostatistics core expert at Washington University. All data are representative of at least two independent experiments unless specifically noted. Sample size was precalculated to satisfy power requirements (with >85% confidence) in most experiments. To accomplish randomization for orthotopic or syngeneic tumor experiments, animals were sorted by a blinded investigator with tumor sizes in ascending order, and then groups were assigned in descending order. Each group was checked *post hoc* to verify no statistical difference in average starting tumor size. Data are shown as mean ± SEM unless otherwise noted. Statistical tests such as unpaired parametric Student $t$ test, ANOVA analysis (Bonferroni multiple comparison), or unpaired nonparametric Mann–Whitney $U$ test were used appropriately based on normality of data. For survival analyses, log-rank (Mantel–Cox) test was used. $P < 0.05$ was considered statistically significant for all studies; ns denotes not significant.

### Data Availability

Bulk-RNA and scRNA-seq data from KPC pancreatic lesions and human PDAC biopsies (NCT04331041) can be found at the Gene Expression Omnibus Repository (GEO) accession numbers GSE207718 and GSE207536. All software packages used are publicly available through commercial vendors.

### Authors' Disclosures

L.-I. Kang reports grants from the NIH during the conduct of the study. J.M. Baer reports grants from the NIH during the conduct of the study. J.K. Schwarz reports receiving NIH grant CA248917 during the conduct of the study, as well as the AACR-Bristol Myers Squibb Female Investigator Grant outside the submitted work. H. Kim reports grants from ViewRay during the conduct of the study, as well as grants and personal fees from Varian outside the submitted work. D.G. DeNardo reports grants from the NIH/NCI during the conduct of the study, as well as grants from Verastem, Bristol Myers Squibb, Pfizer, and PANCAN outside the submitted work. No disclosures were reported by the other authors.

### Authors' Contributions

**V.E. Lander:** Conceptualization, data curation, formal analysis, validation, investigation, visualization, methodology, writing–original draft, writing–review and editing. **J.I. Belle:** Formal analysis, investigation, writing–review and editing. **N.L. Kingston:** Formal analysis, investigation, writing–review and editing. **J.M. Herndon:** Investigation. **G.D. Hogg:** Formal analysis, investigation, writing–review and editing. **X. Liu:** Formal analysis, investigation. **L.-I. Kang:** Formal analysis, investigation, writing–review and editing. **B.L. Knolhoff:** Investigation. **S.J. Bogner:** Investigation. **J.M. Baer:** Investigation, writing–review and editing. **C. Zuo:** Investigation. **N.C. Borcherding:** Formal analysis, methodology. **D.P. Lander:** Data curation, writing–review and editing. **C. Mpoy:** Investigation. **J. Scott:** Investigation. **M. Zahner:** Investigation. **B.E. Rogers:** Resources, supervision, methodology. **J.K. Schwarz:** Conceptualization, resources, supervision, methodology, project administration, writing–review and editing. **H. Kim:** Conceptualization, resources, supervision, methodology, project administration, writing–review and editing. **D.G. DeNardo:** Conceptualization, resources, supervision, funding acquisition, validation, visualization, methodology, project administration, writing–review and editing.

### Acknowledgments

### Note

Supplementary data for this article are available at Cancer Discovery Online (http://cancerdiscovery.aacrjournals.org/).

### REFERENCES

1. Cid-Arregui A, Juarez V. Perspectives in the treatment of pancreatic adenocarcinoma. World J Gastroenterol 2015;21:9297–316.
2. Sarantis P, Koustas E, Papadimitropoulou A, Papavassiliou AG, Karamouzis MV. Pancreatic ductal adenocarcinoma: treatment hurdles, tumor microenvironment and immunotherapy. World J Gastrointest Oncol 2020;12:173–81.
3. McGuigan A, Kelly P, Turkington RC, Jones C, Coleman HG, McCain RS. Pancreatic cancer: a review of clinical diagnosis, epidemiology, treatment and outcomes. World J Gastroenterol 2018;24:4846–61.
4. Hull A, Li Y, Bartholomeusz D, Hsieh W, Allen B, Bezak E. Radioimmunotherapy of pancreatic ductal adenocarcinoma: a review of the current status of literature. Cancers 2020;12:481.

5. Hazard L. The role of radiation therapy in pancreas cancer. Gastrointest Cancer Res 2009;3:20–8.

6. Goodman KA, Hajj C. Role of radiation therapy in the management of pancreatic cancer. J Surg Oncol 2013;107:86–96.

7. Yao W, Maitra A, Ying H. Recent insights into the biology of pancreatic cancer. EBioMedicine 2020;53:102655.

8. Zhang Y, Velez-Delgado A, Mathew E, Li D, Mendez FM, Flannagan K, et al. Myeloid cells are required for PD-1/PD-L1 checkpoint activation and the establishment of an immunosuppressive environment in pancreatic cancer. Gut 2017;66:124–36.

9. Stromnes IM, Brockenbrough JS, Izeradjene K, Carlson MA, Cuevas C, Simmons RM, et al. Targeted depletion of an MDSC subset unmasks pancreatic ductal adenocarcinoma to adaptive immunity. Gut 2014; 63:1769–81.

10. Buscail L, Bournet B, Cordelier P. Role of oncogenic KRAS in the diagnosis, prognosis and treatment of pancreatic cancer. Nat Rev Gastroenterol Hepatol 2020;17:153–68.

11. Valkenburg KC, De Groot AE, Pienta KJ. Targeting the tumour stroma to improve cancer therapy. Nat Rev Clin Oncol 2018;15:366–81.

12. Krisnawan VE, Stanley JA, Schwarz JK, DeNardo DG. Tumor microenvironment as a regulator of radiation therapy: new insights into stromal-mediated radioresistance. Cancers (Basel) 2020;12:2916.

13. Chen Y, McAndrews KM, Kalluri R. Clinical and therapeutic relevance of cancer-associated fibroblasts. Nat Rev Clin Oncol 2021;18:792–804.

14. Öhlund D, Handly-Santana A, Biffi G, Elyada E, Almeida AS, Ponz-Sarvise M, et al. Distinct populations of inflammatory fibroblasts and myofibroblasts in pancreatic cancer. J Exp Med 2017;214:579–96.

15. Ohlund D, Lundin C, Ardnor B, Oman M, Naredi P, Sund M. Type IV collagen is a tumour stroma-derived biomarker for pancreas cancer. Br J Cancer 2009;101:91–7.

16. Whatcott CJ, Diep CH, Jiang P, Watanabe A, LoBello J, Sima C, et al. Desmoplasia in primary tumors and metastatic lesions of pancreatic cancer. Clin Cancer Res 2015;21:3561–8.

17. Feig C, Gopinathan A, Neesse A, Chan DS, Cook N, Tuveson DA. The pancreas cancer microenvironment. Clin Cancer Res 2012;18:4266–76.

18. Leca J, Martinez S, Lac S, Nigri J, Secq V, Rubis M, et al. Cancer-associated fibroblast-derived annexin A6+ extracellular vesicles support pancreatic cancer aggressiveness. J Clin Invest 2016;126:4140–56.

19. Gandhi L, Rodríguez-Abreu D, Gadgeel S, Esteban E, Felip E, De Angelis F, et al. Pembrolizumab plus chemotherapy in metastatic non–small-cell lung cancer. N Engl J Med 2018;378:2078–92.

20. Larkin J, Chiarion-Sileni V, Gonzalez R, Grob JJ, Cowey CL, Lao CD, et al. Combined nivolumab and ipilimumab or monotherapy in untreated melanoma. N Engl J Med 2015;373:23–34.

21. Robert C, Schachter J, Long GV, Arance A, Grob JJ, Mortier L, et al. Pembrolizumab versus ipilimumab in advanced melanoma. N Engl J Med 2015;372:2521–32.

22. Kunk PR, Bauer TW, Slingluff CL, Rahma OE. From bench to bedside a comprehensive review of pancreatic cancer immunotherapy. J Immunother Cancer 2016;4:14.

23. O'Reilly EM, Oh D-Y, Dhani N, Renouf DJ, Lee MA, Sun W, et al. Durvalumab with or without tremelimumab for patients with metastatic pancreatic ductal adenocarcinoma: a phase 2 randomized clinical trial. JAMA Oncol 2019;5:1431–8.

24. Neoptolemos JP, Stocken DD, Friess H, Bassi C, Dunn JA, Hickey H, et al. A randomized trial of chemoradiotherapy and chemotherapy after resection of pancreatic cancer. N Engl J Med 2004;350:1200–10.

25. Wainberg ZA, Hochster HS, Kim EJ, George B, Kaylan A, Chiorean EG, et al. Open-label, phase I study of nivolumab combined with nab-paclitaxel plus gemcitabine in advanced pancreatic cancer. Clin Cancer Res 2020;26:4814.

26. Gajiwala S, Torgeson A, Garrido-Laguna I, Kinsey C, Lloyd S. Combination immunotherapy and radiation therapy strategies for pancreatic cancer: targeting multiple steps in the cancer immunity cycle. Journal of Gastrointestinal Oncology 2018;9:1014–26.

27. Biffi G, Tuveson DA. Diversity and biology of cancer-associated fibroblasts. Physiol Rev 2021;101:147–76.

28. Biffi G, Oni TE, Spielman B, Hao Y, Elyada E, Park Y, et al. IL1-induced JAK/STAT signaling is antagonized by TGFβ to shape CAF heterogeneity in pancreatic ductal adenocarcinoma. Cancer Discov 2019;9:282.

29. Elyada E, Bolisetty M, Laise P, Flynn WF, Courtois ET, Burkhart RA, et al. Cross-species single-cell analysis of pancreatic ductal adenocarcinoma reveals antigen-presenting cancer-associated fibroblasts. Cancer Discov 2019;9:1102–23.

30. Nieskoski MD, Marra K, Gunn JR, Hoopes PJ, Doyley MM, Hasan T, et al. Collagen complexity spatially defines microregions of total tissue pressure in pancreatic cancer. Sci Rep 2017;7:10093.

31. Trédan O, Galmarini CM, Patel K, Tannock IF. Drug resistance and the solid tumor microenvironment. J Natl Cancer Inst 2007;99:1441–54.

32. Netti PA, Berk DA, Swartz MA, Grodzinsky AJ, Jain RK. Role of extracellular matrix assembly in interstitial transport in solid tumors. Cancer Res 2000;60:2497–503.

33. DuFort CC, DelGiorno KE, Carlson MA, Osgood RJ, Zhao C, Huang Z, et al. Interstitial pressure in pancreatic ductal adenocarcinoma is dominated by a Gel-fluid phase. Biophys J 2016;110:2106–19.

34. Baskar R, Dai J, Wenlong N, Yeo R, Yeoh K-W. Biological response of cancer cells to radiation treatment. Front Mol Biosci 2014;1:24.

35. Deng M, Lin J, Nowsheen S, Liu T, Zhao Y, Villalta PW, et al. Extracellular matrix stiffness determines DNA repair efficiency and cellular sensitivity to genotoxic agents. Sci Adv;6:eabb2630.

36. Deville SS, Cordes N. The extracellular, cellular, and nuclear stiffness, a trinity in the cancer resistome—a review. Front Oncol 2019;9:1376.

37. Kaur P, Asea A. Radiation-induced effects and the immune system in cancer. Front Oncol 2012;2:191.

38. Serrels A, Lund T, Serrels B, Byron A, McPherson Rhoanne C, von Kriegsheim A, et al. Nuclear FAK controls chemokine transcription, tregs, and evasion of anti-tumor immunity. Cell 2015;163:160–73.

39. Sulzmaier FJ, Jean C, Schlaepfer DD. FAK in cancer: mechanistic findings and clinical applications. Nat Rev Cancer 2014;14:598–610.

40. Tavora B, Reynolds LE, Batista S, Demircioglu F, Fernandez I, Lechertier T, et al. Endothelial-cell FAK targeting sensitizes tumours to DNA-damaging therapy. Nature 2014;514:112–6.

41. Zhao X-K, Cheng Y, Cheng ML, Yu L, Mu M, Li H, et al. Focal adhesion kinase regulates fibroblast migration via integrin beta-1 and plays a central role in fibrosis. Sci Rep 2016;6:19276.

42. Stokes JB, Adair SJ, Slack-Davis JK, Walters DM, Tilghman RW, Hershey ED, et al. Inhibition of focal adhesion kinase by PF-562,271 inhibits the growth and metastasis of pancreatic cancer concomitant with altering the tumor microenvironment. Mol Cancer Ther 2011;10:2135–45.

43. Schlaepfer DD, Hunter T. Signal transduction from the extracellular matrix—a role for the focal adhesion protein-tyrosine kinase FAK. Cell Struct Funct 1996;21:445–50.

44. Mitra SK, Hanson DA, Schlaepfer DD. Focal adhesion kinase: in command and control of cell motility. Nat Rev Mol Cell Biol 2005;6:56–68.

45. Jiang H, Hegde S, DeNardo DG. Tumor-associated fibrosis as a regulator of tumor immunity and response to immunotherapy. Cancer Immunol Immunother 2017;66:1037–48.

46. Jiang H, Hegde S, Knolhoff BL, Zhu Y, Herndon JM, Meyer MA, et al. Targeting focal adhesion kinase renders pancreatic cancers responsive to checkpoint immunotherapy. Nat Med 2016;22:851–60.

47. Laklai H, Miroshnikova YA, Pickup MW, Collisson EA, Kim GE, Barrett AS, et al. Genotype tunes pancreatic ductal adenocarcinoma tissue tension to induce matricellular fibrosis and tumor progression. Nat Med 2016;22:497–505.

48. Venkatesulu BP, Hsieh C-E, Sanders KL, Krishnan S. Recent advances in radiation therapy of pancreatic cancer. F1000Res 2018;7:F1000.

49. Li D, Xie K, Wolff R, Abbruzzese JL. Pancreatic cancer. Lancet North Am Ed 2004;363:1049–57.

50. Hingorani SR, Wang L, Multani AS, Combs C, Deramaudt TB, Hruban RH, et al. Trp53R172H and KrasG12D cooperate to promote chromosomal instability and widely metastatic pancreatic ductal adenocarcinoma in mice. Cancer Cell 2005;7:469–83.

51. Wong J, Armour E, Kazanzides P, Iordachita I, Tryggestad E, Deng H, et al. High-resolution, small animal radiation research platform with x-ray tomographic guidance capabilities. Int J Radiat Oncol Biol Phys 2008;71:1591–9.

52. Seifert L, Werba G, Tiwari S, Ly NNG, Nguy S, Alothman S, et al. Radiation therapy induces macrophages to suppress T-cell responses against pancreatic tumors in mice. Gastroenterology 2016;150:1659–72.

53. Mills BN, Connolly KA, Ye J, Murphy JD, Uccello TP, Han BJ, et al. Stereotactic body radiation and Interleukin-12 combination therapy eradicates pancreatic tumors by repolarizing the immune microenvironment. Cell Rep 2019;29:406–21.

54. Hegde S, Krisnawan VE, Herzog BH, Zuo C, Breden MA, Knolhoff BL, et al. Dendritic cell paucity leads to dysfunctional immune surveillance in pancreatic cancer. Cancer Cell 2020;37:289–307.

55. Kirsch DG, Dinulescu DM, Miller JB, Grimm J, Santiago PM, Young NP, et al. A spatially and temporally restricted mouse model of soft tissue sarcoma. Nat Med 2007;13:992–7.

56. Thomas D, Radhakrishnan P. Tumor-stromal crosstalk in pancreatic cancer and tissue fibrosis. Mol Cancer 2019;18:14.

57. Apte MV, Park S, Phillips PA, Santucci N, Goldstein D, Kumar RK, et al. Desmoplastic reaction in pancreatic cancer: role of pancreatic stellate cells. Pancreas 2004;29:179–87.

58. Park CC, Zhang H, Pallavicini M, Gray JW, Baehner F, Park CJ, et al. Β1 integrin inhibitory antibody induces apoptosis of breast cancer cells, inhibits growth, and distinguishes malignant from normal phenotype in three-dimensional cultures and in vivo. Cancer Res 2006;66:1526–35.

59. Park CC, Zhang HJ, Yao ES, Park CJ, Bissell MJ. Β1 integrin inhibition dramatically enhances radiotherapy efficacy in human breast cancer xenografts. Cancer Res 2008;68:4398–405.

60. Cordes N, Seidler J, Durzok R, Geinitz H, Brakebusch C. Β1-integrin-mediated signaling essentially contributes to cell survival after radiation-induced genotoxic injury. Oncogene 2006;25:1378–90.

61. Feig C, Jones JO, Kraman M, Wells RJB, Deonarine A, Chan DS, et al. Targeting CXCL12 from FAP-expressing carcinoma-associated fibroblasts synergizes with anti–PD-L1 immunotherapy in pancreatic cancer. Proc Natl Acad Sci 2013;110:20212.

62. Hutton C, Heider F, Blanco-Gomez A, Banyard A, Kononov A, Zhang X, et al. Single-cell analysis defines a pancreatic fibroblast lineage that supports anti-tumor immunity. Cancer Cell 2021;39:1227–44.

63. Dominguez CX, Müller S, Keerthivasan S, Koeppen H, Hung J, Gierke S, et al. Single-cell RNA sequencing reveals stromal evolution into LRRC15(+) myofibroblasts as a determinant of patient response to cancer immunotherapy. Cancer Discov 2020;10:232–53.

64. Francescone R, Vendramini-Costa DB, Franco-Barraza J, Wagner J, Muir A, Lau AN, et al. Netrin G1 promotes pancreatic tumorigenesis through cancer-associated fibroblast-driven nutritional support and immunosuppression. Cancer Discov 2021;11:446–79.

65. Helms EJ, Berry MW, Chaw RC, DuFort CC, Sun D, Onate MK, et al. Mesenchymal lineage heterogeneity underlies nonredundant functions of pancreatic cancer–associated fibroblasts. Cancer Discov 2022;12:484–501.

66. Cordes N. Integrin-mediated cell-matrix interactions for prosurvival and antiapoptotic signaling after genotoxic injury. Cancer Lett 2006;242:11–9.

67. Goel HL, Sayeed A, Breen M, Zarif MJ, Garlick DS, Leav I, et al. β1 integrins mediate resistance to ionizing radiation in vivo by inhibiting c-Jun amino terminal kinase 1. J Cell Physiol 2013;228:1601–9.

68. Klein D, Schmitz T, Verhelst V, Panic A, Schenck M, Reis H, et al. Endothelial Caveolin-1 regulates the radiation response of epithelial prostate tumors. Oncogenesis 2015;4:e148.

69. Weichselbaum RR, Ishwaran H, Yoon T, Nuyten DSA, Baker SW, Khodarev N, et al. An interferon-related gene signature for DNA damage resistance is a predictive marker for chemotherapy and radiation for breast cancer. Proc Nat Acad Sci USA 2008;105:18490–5.

70. Puthawala K, Hadjiangelis N, Jacoby SC, Bayongan E, Zhao Z, Yang Z, et al. Inhibition of integrin αvβ6, an activator of latent transforming growth factor-β, prevents radiation-induced lung fibrosis. Am J Respir Crit Care Med 2008;177:82–90.

71. Chetty C, Bhoopathi P, Rao JS, Lakka SS. Inhibition of matrix metalloproteinase-2 enhances radiosensitivity by abrogating radiation-induced FoxM1-mediated G2–M arrest in A549 lung cancer cells. Int J Cancer 2009;124:2468–77.

72. Biswas S, Freeman ML, Arteaga CL, Biswas S, Guix M, Rinehart C, et al. Inhibition of TGF beta with neutralizing antibodies prevents radiation-induced acceleration of metastatic cancer progression Find the latest version: inhibition of TGF-β with neutralizing antibodies

73. prevents radiation-induced acceleration of metastatic. J Clin Invest 2007;117:1305–13.

73. Hellevik T, Martinez-Zubiaurre I. Radiotherapy and the tumor stroma: the importance of dose and fractionation. Front Oncol 2014;4:1–12.

74. Ansiaux R, Baudelet C, Jordan BF, Beghein N, Sonveaux P, De Wever J, et al. Thalidomide radiosensitizes tumors through early changes in the tumor microenvironment. Clin Cancer Res 2005;11:743–50.

75. Crokart N, Jordan BF, Baudelet C, Ansiaux R, Sonveaux P, Grégoire V, et al. Early reoxygenation in tumors after irradiation: determining factors and consequences for radiotherapy regimens using daily multiple fractions. Int J Radiat Oncol Biol Phys 2005;63:901–10.

76. Gupta A, Probst HC, Vuong V, Landshammer A, Muth S, Yagita H, et al. Radiotherapy promotes tumor-specific effector CD8+ T cells via dendritic cell activation. J Immunol 2012;189:558–66.

77. Lee Y, Auh SL, Wang Y, Burnette B, Wang Y, Meng Y, et al. Therapeutic effects of ablative radiation on local tumor require CD8+ T cells: changing strategies for cancer treatment. Blood 2009;114:589–95.

78. Hwang RF, Moore T, Arumugam T, Ramachandran V, Amos KD, Rivera A, et al. Cancer-associated stromal fibroblasts promote pancreatic tumor progression. Cancer Res 2008;68:918–26.

79. Mantoni TS, Lunardi S, Al-Assar O, Masamune A, Brunner TB. Pancreatic stellate cells radioprotect pancreatic cancer cells through β1-integrin signaling. Cancer Res 2011;71:3453–8.

80. Sasson AR, Wetherington RW, Hoffman JP, Ross EA, Cooper H, Meropol NJ, et al. Neoadjuvant chemoradiotherapy for adenocarcinoma of the pancreas. Int J Gastrointest Cancer 2003;34:121–7.

81. Chun YS, Cooper HS, Cohen SJ, Konski A, Burtness B, Denlinger CS, et al. Significance of pathologic response to preoperative therapy in pancreatic cancer. Ann Surg Oncol 2011;18:3601–7.

82. Dawson JC, Serrels A, Stupack DG, Schlaepfer DD, Frame MC. Targeting FAK in anticancer combination therapies. Nat Rev Cancer 2021;21:313–24.

83. Tang K-J, Constanzo JD, Venkateswaran N, Melegari M, Ilcheva M, Morales JC, et al. Focal adhesion kinase regulates the DNA damage response and its inhibition radiosensitizes mutant KRAS lung cancer. Clin Cancer Res 2016;22:5851–63.

84. Özdemir BC, Pentcheva-Hoang T, Carstens JL, Zheng X, Wu CC, Simpson TR, et al. Depletion of carcinoma-associated fibroblasts and fibrosis induces immunosuppression and accelerates pancreas cancer with reduced survival. Cancer Cell 2014;25:719–34.

85. Chen Y, Kim J, Yang S, Wang H, Wu C-J, Sugimoto H, et al. Type I collagen deletion in αSMA+ myofibroblasts augments immune suppression and accelerates progression of pancreatic cancer. Cancer Cell 2021;39:548–65.

86. Lo A, Li C-P, Buza EL, Blomberg R, Govindaraju P, Avery D, et al. Fibroblast activation protein augments progression and metastasis of pancreatic ductal adenocarcinoma. JCI Insight 2017;2:e92232.

87. McAndrews KM, Chen Y, Darpolor JK, Zheng X, Yang S, Carstens JL, et al. Identification of functional heterogeneity of carcinoma-associated fibroblasts with distinct IL-6 mediated therapy resistance in pancreatic cancer. Cancer Discov 2022;12:1580–97.

88. Boj SF, Hwang C-I, Baker LA, Chio IIC, Engle DD, Corbo V, et al. Organoid models of human and mouse ductal pancreatic cancer. Cell 2015;160:324–38.

89. Kim MP, Evans DB, Wang H, Abbruzzese JL, Fleming JB, Gallick GE. Generation of orthotopic and heterotopic human pancreatic cancer xenografts in immunodeficient mice. Nat Protoc 2009;4:1670–80.

90. Hafemeister C, Satija R. Normalization and variance stabilization of single-cell RNA-seq data using regularized negative binomial regression. Genome Biol 2019;20:296.

91. Korsunsky I, Millard N, Fan J, Slowikowski K, Zhang F, Wei K, et al. Fast, sensitive and accurate integration of single-cell data with Harmony. Nat Methods 2019;16:1289–96.

92. Wu T, Hu E, Xu S, Chen M, Guo P, Dai Z, et al. clusterProfiler 4.0: a universal enrichment tool for interpreting omics data. Innovation (Camb) 2021;2:100141.

93. Tsujikawa T, Kumar S, Borkar RN, Azimi V, Thibault G, Chang YH, et al. Quantitative multiplex immunohistochemistry reveals myeloid-inflamed tumor-immune complexity associated with poor prognosis. Cell Rep 2017;19:203–17.